Characterization of Proton Irradiated SiC Sensors

Summer Student Project in the EP-DT-DD SSD Group at CERN

Elias Arnqvist*

Supervisors:
Moritz Wiehe†
Michael Moll‡

2023-08-25

*Uppsala University, Sweden
†CERN
‡CERN

Abstract

The large bandgap semiconductor silicon carbide (SiC) has properties that make it attractive for use in sensors in particle detectors at CERN. For instance, it has a lower leakage current and could be more radiation hard than silicon (Si). This project aims to study SiC sensors and determine their characteristics before and after 24 GeV/c proton irradiation. Current-voltage, capacitance-voltage, and charge collection efficiency measurements were performed for 5 µm and 50 µm thick SiC sensors manufactured by IMB-CNM. The charge collection measurements were done with an ultraviolet (375 nm) transient current technique setup. A calibration of this setup was also performed. Results show an increasing forward junction potential and no change in reverse leakage current with irradiation, but higher voltage and lower current reverse bias measurements are needed. The capacitance as a function of bias voltage flattens out with increasing proton irradiation, indicating that diode properties are lost. The charge collection efficiency was found to decrease with irradiation.

Acknowledgements

I want to express my deep gratitude to my supervisor Moritz Wiehe for his help and guidance, in addition to converting many files from `.txt` to `.root`. Furthermore, I want to thank my supervisor Michael Moll for this opportunity and for the office fan that made the warm Geneva summer less unbearable. A big thank you goes to the whole SSD group at CERN for 3D-printed geckos, help with putting sensors in irradiation cards, assistance with ROOT, and many other things.

I am also grateful to Joan Marc Rafí at IMB-CNM for the SiC sensors that were studied in this project. Moreover, I want to thank Giuseppe Pezzullo at PS-IRRAD at CERN for his help in irradiating the sensors and for the tour of the IRRAD facility.

Finally, thank you CERN for an unforgettable summer.

Contents

1 Introduction

The purpose of this report is to summarize the project performed by the author during his participation in the CERN Summer Student Program 2023. The project was conducted in the EP-DT-DD Solid State Detector (SSD) group at CERN. In general, this report focuses on showing the obtained results and conclusions. Due to time limitations, some details and measurements are omitted.

1.1 Background

Detectors play an essential role in experiments at CERN. For instance, semiconductor detectors make it possible to track high-energy particles accurately, resulting in reconstructions of particle paths used for particle physics analysis. Most semiconductor detectors used today are made from silicon (Si) sensors. However, interest in silicon carbide (SiC) sensors has been sparked by recent developments in fabrication technology. This project aims to study SiC sensors and characterize how they are affected by proton radiation.

Differences between Si and SiC semiconductors are presented in table 1. Only sensors made from the 4H-SiC polymorph are studied in this project. The term SiC in this report refers to 4H-SiC.

Table 1: Selected properties of Si and SiC (at 300 K) [1].

Property	Si	SiC
Bandgap (eV)	1.12	3.27
e-h pair creation energy (eV)	3.6	7.6-8.4
Threshold displacement energy (eV)	13-15	30-40
Electron saturation velocity (cm/s)	$0.8 \cdot 10^7$	$2 \cdot 10^7$
Breakdown electric field (V/cm)	$3 \cdot 10^5$	3-4$\cdot 10^6$
Electron mobility (cm^2/Vs)	1450	800
Hole mobility (cm^2/Vs)	450	115
Relative permittivity, ε_r	11.9	9.7

SiC semiconductors have an almost three times larger bandgap than Si. A beneficial consequence of a large bandgap is a low leakage current. The leakage current density under reverse bias J_R is

$$|J_R| \approx J_0 \propto T^{(3+\gamma/2)} \exp\left(-\frac{E_g}{k_B T}\right), \tag{1}$$

where T is the temperature, γ is a constant, k_B is the Boltzmann constant, and E_g is the bandgap (see p. 95 in [2]). A low leakage current results in low power consumption and less cooling. This is a reason why SiC is attractive for particle detector applications.

The threshold displacement energy is the energy needed to displace an atom in a lattice to a defect position. The higher threshold displacement energy of SiC could imply that it is more radiation hard. However, having two atoms in the lattice as opposed to one (as in Si) might counteract this. This needs to be investigated further.

1.2 Sensors

SiC sensors manufactured by IMB-CNM (Spain) were obtained. Of the sensors, 10 were 5 µm thick and 14 were 50 µm thick. The sensors were either divided up into 4 identical quadrants or have one full planar pad. Moreover, the sensors had either metalized or non-metalized surfaces. A sensor cross-section is shown in figure 2. Pictures of different types of sensors are shown in figure 3.

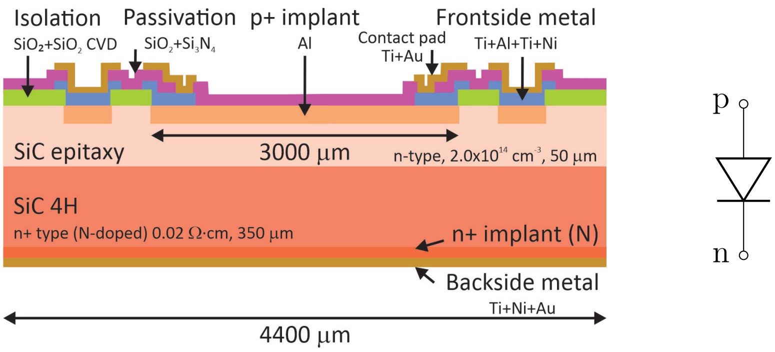

Figure 2: Cross-section of one of the 50 µm thick SiC sensors.

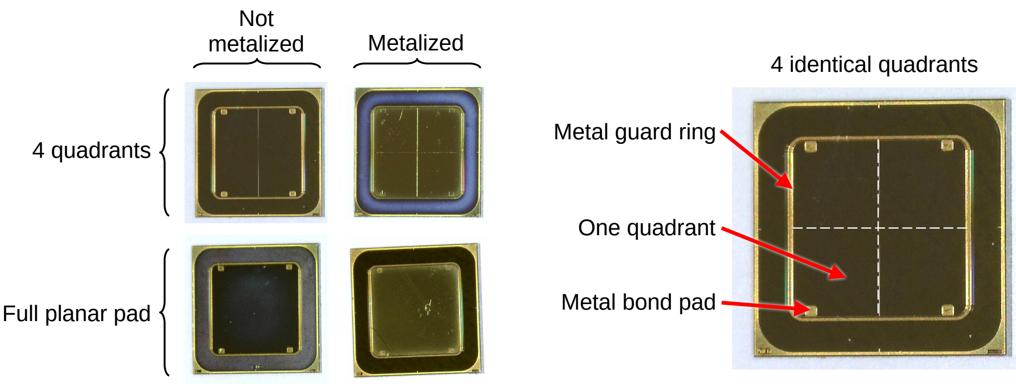

Figure 3: Examples of some of the studied SiC sensors.

The sensors are, in other words, diodes with a p^+n-junction. The p^+n-junction is formed between the p^+-type (Al doped) implant layer and the SiC n-type (N doped, $N_d = 2 \cdot 10^{14} \text{cm}^{-3}$) epitaxy in figure 2.

A full list of the sensors that were studied in this project is shown in table 2. Figure 4 is a key to the sensor naming system that was used.

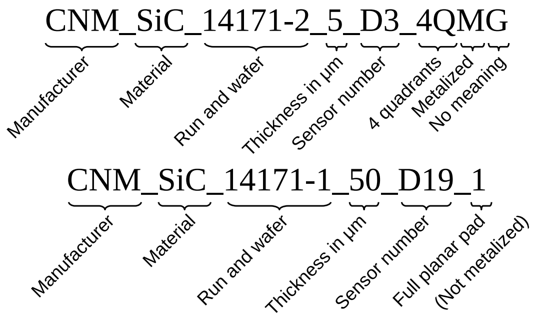

Figure 4: Key to SiC sensor naming system.

Table 2: All studied SiC sensors, in addition to some properties.

Sensor name	Thickness (µm)	Layout	Metalized
CNM_SiC_14171-2_5_D6_4QG	5	4 quadrants	no
CNM_SiC_14171-2_5_D5_4Q	5	4 quadrants	no
CNM_SiC_14171-2_5_D2_4QG	5	4 quadrants	no
CNM_SiC_14171-2_5_D13_1	5	full planar pad	no
CNM_SiC_14171-2_5_D11_1	5	full planar pad	no
CNM_SiC_14171-2_5_D7_4QMG	5	4 quadrants	yes
CNM_SiC_14171-2_5_D4_4QM	5	4 quadrants	yes
CNM_SiC_14171-2_5_D3_4QMG	5	4 quadrants	yes
CNM_SiC_14171-2_5_D12_1M	5	full planar pad	yes
CNM_SiC_14171-2_5_D14_1M	5	full planar pad	yes
CNM_SiC_14171-1_50_D9_4Q	50	4 quadrants	no
CNM_SiC_14171-1_50_D5_4Q	50	4 quadrants	no
CNM_SiC_14171-1_50_D2_4QG	50	4 quadrants	no
CNM_SiC_14171-1_50_D13_4Q	50	4 quadrants	no
CNM_SiC_14171-1_50_D10_4QG	50	4 quadrants	no
CNM_SiC_14171-1_50_D1_4Q	50	4 quadrants	no
CNM_SiC_14171-1_50_D19_1	50	full planar pad	no
CNM_SiC_14171-1_50_D7_4QMG	50	4 quadrants	yes
CNM_SiC_14171-1_50_D16_4QM	50	4 quadrants	yes
CNM_SiC_14171-1_50_D12_4QM	50	4 quadrants	yes
CNM_SiC_14171-1_50_D11_4QMG	50	4 quadrants	yes
CNM_SiC_14171-1_50_D22_1M	50	full planar pad	yes
CNM_SiC_14171-1_50_D20_1M	50	full planar pad	yes
CNM_SiC_14171-1_50_D18_1M	50	full planar pad	yes

1.3 Irradiation

Some of the sensors were irradiated at the PS-IRRAD facility at CERN. There, they were irradiated by 24 GeV/c protons from the Proton Synchrotron accelerator at CERN. Fluences of 10^{13}, 10^{14}, and 10^{15} protons/cm^2 (p/cm^2) were used. The sensors selected to be irradiated are shown in table 3. Sensors were stored at -20 °C after irradiation to prevent annealing.

Table 3: All SiC sensors that were irradiated.

Sensor name	Fluence (p/cm^2)
CNM_SiC_14171-2_5_D6_4QG	10^{13}
CNM_SiC_14171-2_5_D5_4Q	10^{14}
CNM_SiC_14171-2_5_D2_4QG	10^{15}
CNM_SiC_14171-2_5_D12_1M	10^{13}
CNM_SiC_14171-2_5_D14_1M	10^{14}
CNM_SiC_14171-1_50_D9_4Q	10^{13}
CNM_SiC_14171-1_50_D5_4Q	10^{14}
CNM_SiC_14171-1_50_D2_4QG	10^{15}
CNM_SiC_14171-1_50_D20_1M	10^{13}
CNM_SiC_14171-1_50_D18_1M	10^{14}

1.4 Measurements

Measurements were conducted on sensors without radiation and with varying fluences to determine how their properties had changed. Current-voltage and capacitance-voltage measurements were performed. Transient current technique measurements were also done. Defect spectroscopy measurements were started, but due to time constraints, these results will not be presented here. Results are shown in corresponding sections below.

2 Current-Voltage and Capacitance-Voltage

This section describes the current-voltage (IV) and capacitance-voltage (CV) measurements that were performed. The goal was to compare IV- and CV-characteristics between unirradiated and irradiated sensors. Typical characteristics of the unirradiated sensors are also shown below.

2.1 Background

A reverse biased diode will conduct a leakage current, according to equation 1. A sufficiently large electric field across the pn-junction will cause the pn-junction to break down and conduct a very large current. The voltage at which this happens is known as the breakdown voltage. In forward bias, the voltage needed for the conduction of current is called the forward junction potential.

The capacitance C of the depletion region of a reverse biased pn-junction is

$$C = \frac{\varepsilon_s A}{W} \approx A\sqrt{\frac{q\varepsilon_s N_{eff}}{2V_{bias}}}, \tag{2}$$

where ε_s is the permittivity, A is the junction area, W is the depletion region width, q is the elementary charge, N_{eff} is the effective doping concentration, and V_{bias} is the bias voltage. For a p$^+$n-junction, such as in figure 2,

$$N_{eff} = \frac{N_a N_d}{N_a + N_d} \approx N_d, \tag{3}$$

as $N_a \gg N_d$. The depletion voltage V_{dep} is the voltage at which W cannot increase further and the junction has reached full depletion.

A consequence of equation 2 is that

$$\frac{1}{C^2} \approx \frac{2V_{bias}}{qN_{eff}\varepsilon_s A^2} = slope \cdot V_{bias} \quad \Rightarrow \quad N_{eff} \approx \frac{2}{q\varepsilon_s A^2 \cdot slope}, \tag{4}$$

so one can extract N_{eff} from the slope if one plots $1/C^2$ as a function of V_{bias}. Furthermore, since the capacitance at V_{dep} is

$$C_{dep} \approx A\sqrt{\frac{q\varepsilon_s N_{eff}}{2V_{dep}}} \quad \Rightarrow \quad N_{eff} \approx \frac{C_{dep}^2 V_{dep}}{A^2 q\varepsilon_s}, \tag{5}$$

so N_{eff} can be determined from C_{dep} and V_{dep}. Equations in this section can be found in [2].

2.2 Method

IV- and CV-measurements were conducted in the SSD lab at CERN. Most measurements were performed at the IVCV probe station. Some measurements were performed on the TCT- setup. During these measurements, the bias voltage V_{bias} is defined as is figure 5. Consequently, $V_{bias} > 0$ means reverse biased and $V_{bias} < 0$ means forward biased.

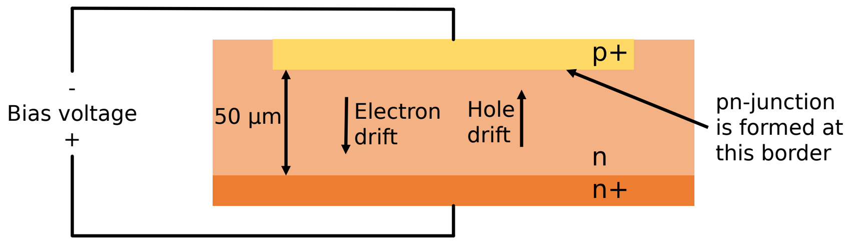

Figure 5: SiC sensor and V_{bias}.

The areas of the sensors were determined to be 0.02255 cm^2 for one quadrant (on 4 quadrant samples) and 0.08982 cm^2 for a full planar pad. These numbers were calculated from a technical drawing of the sensor layout.

All IV-measurements are shown in appendix A. Most sensors had similar breakdown voltages. These were >1000 V for 50 µm sensors and ≈120 V for 5 µm sensors. The voltage supply was limited to 1000 V. However, the breakdown voltage of some sensors deviated from these values. The forward junction potential was more consistent, and about 1.8 V for both thicknesses.

It was discovered that the voltage ramping speed of the IV-measurement greatly affected the measured leakage currents. These measurements are shown in appendix B. Slow ramping speeds of 0.1 V/s were required to measure the leakage current accurately. No difference was observed for slow measurements at 20 °C and -20 °C.

CV-measurements were found to be consistent between diodes of the same thickness and area. Typical measurements are shown in appendix C. For 50 µm sensors, values of V_{dep} were about 340 V. Values of N_{eff} calculated from the slope of $1/C^2$-plots and from V_{dep} match the expected $2 \cdot 10^{14}$ cm^{-3}. The full depletion width was found to be between 40-50 µm. For 5 µm sensors, results were less clear. These sensors are nearly fully depleted at 0 V and the junction extends into the bulk semiconductor material at low V_{bias}.

2.3 Results

In this section, IV- and CV-characteristics of unirradiated and irradiated sensors are presented.

2.3.1 50 µm sensors

An IV-measurement for both reverse and forward biased sensors is shown in figure 6. Figures 7 and 8 show CV-characteristics of the sensors.

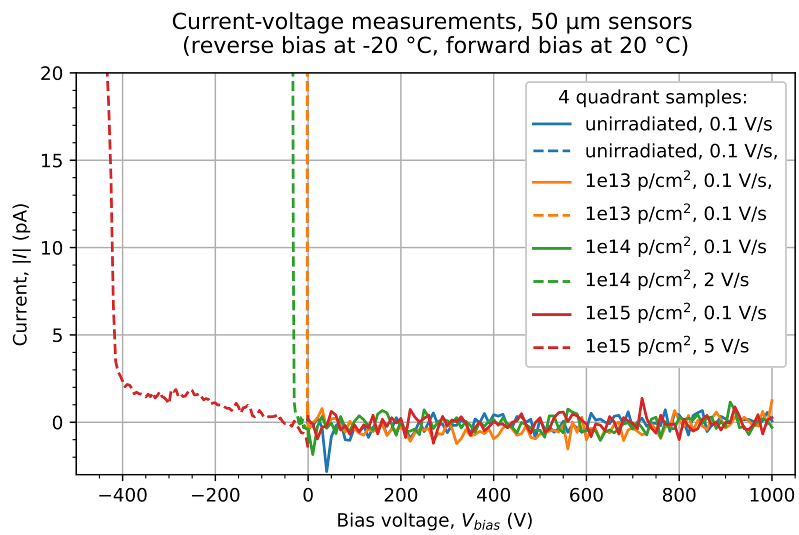

Figure 6: Current-voltage measurements for 4 quadrant, 50 µm thick sensors.

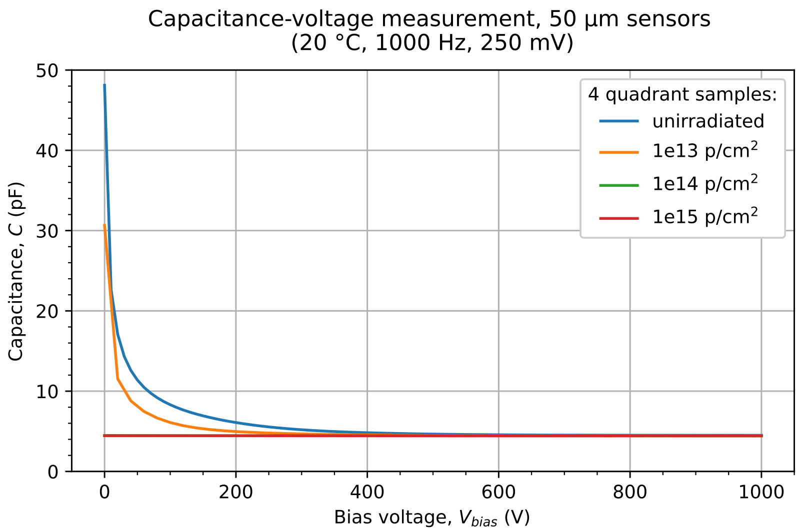

Figure 7: Capacitance-voltage measurements for 4 quadrant, 50 µm thick sensors.

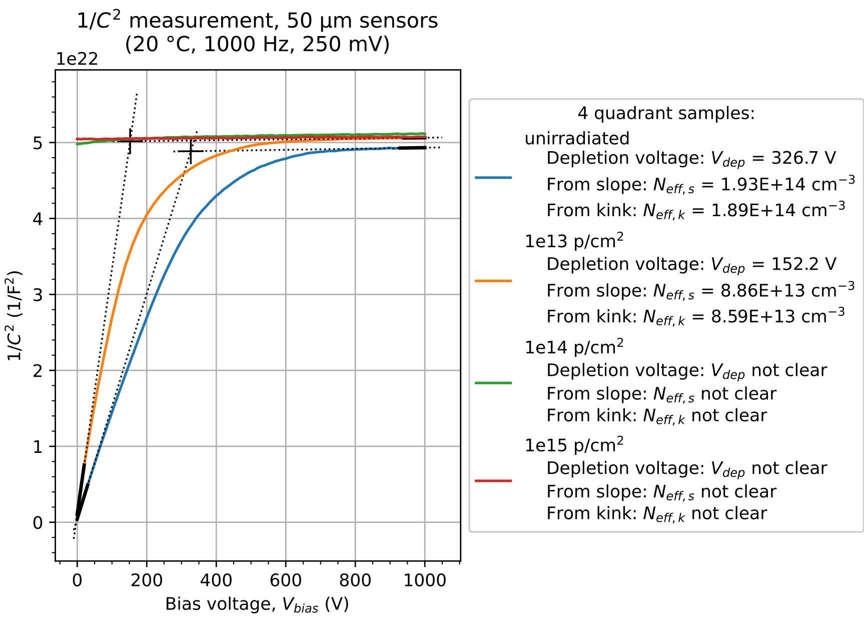

Figure 8: $1/C^2$-plots for 4 quadrant, 50 µm thick sensors.

2.3.2 5 µm sensors

IV-measurements for reverse and forward biased sensors are shown in figures 9 and 10, respectively. Figures 11 and 12 show CV-characteristics of the sensors.

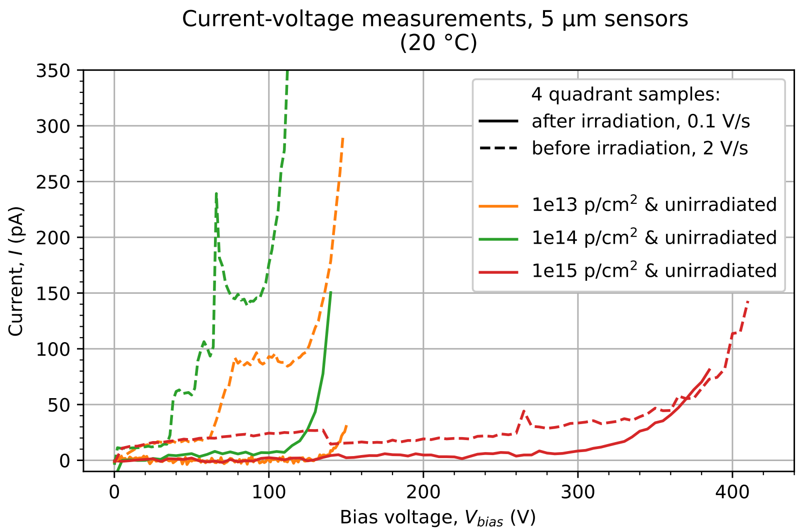

Figure 9: Current-voltage measurements (reverse bias) for 4 quadrant, 5 µm thick sensors.

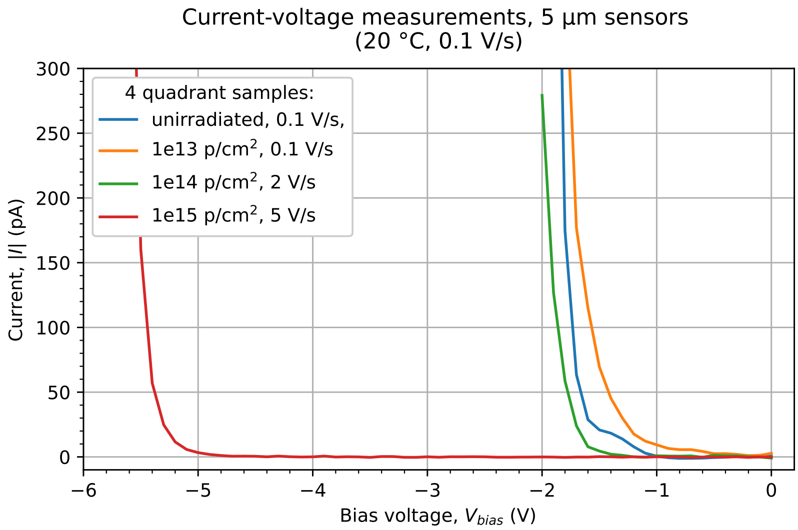

Figure 10: Current-voltage measurements (forward bias) for 4 quadrant, 5 µm thick sensors.

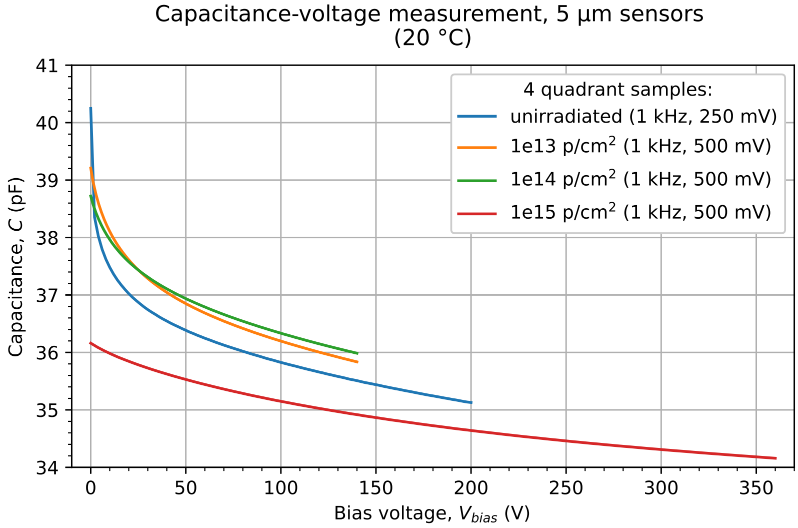

Figure 11: Capacitance-voltage measurements for 4 quadrant, 5 µm thick sensors.

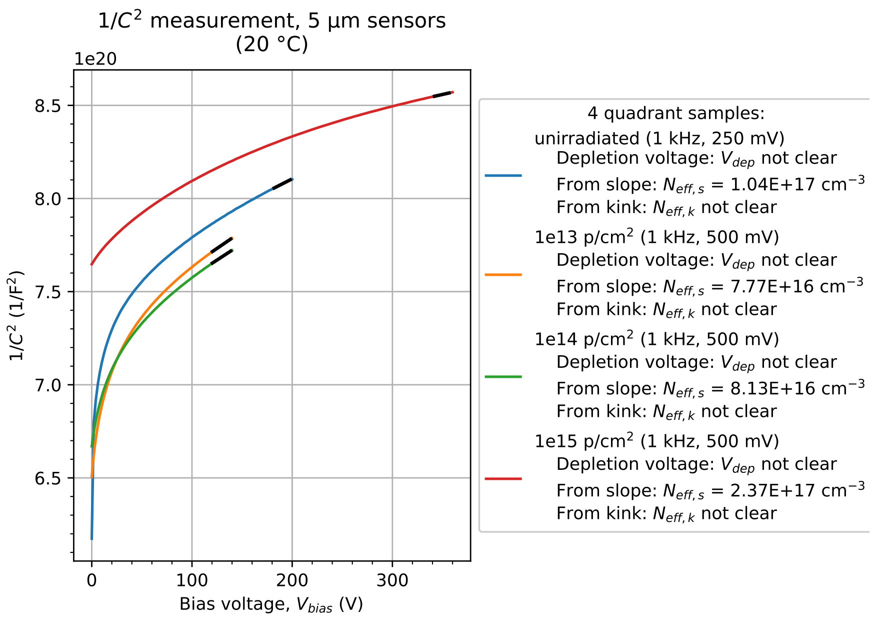

Figure 12: $1/C^2$-plots for 4 quadrant, 5 µm thick sensors.

2.4 Discussion

For 50 µm sensors under reverse bias, the leakage currents were found to be extremely low. Note that the reverse bias measurements were performed at -20 °C (to prevent annealing during the 6 hour measurement). However, this should not make a difference when compared to 20 °C (see appendix B). The break down voltage was not reached for the irradiated samples, as these sensors initially had break down voltages >1000 V as well.

The behavior of 50 µm sensors change under forward bias, after irradiation. The forward junction potential changes from about 1.8 V for the unirradiated sensor to more than 400 V for the 10^{15} p/cm^2 sensor.

The CV-curves of the 50 µm sensors appear to flatten out with irradiation. This indicates that their diode properties are lost. The $1/C^2$-plot indicates that the V_{dep} decreases with irradiation and that N_{eff} decreases with irradiation. However, if the sensor after irradiation no longer can be seen as an ideal diode, then the estimated N_{eff} values could be inaccurate.

For 5 µm sensors under reverse bias, leakage currents are again low. The difference between unirradiated and irradiated curves is attributed to the ramping speed difference. The breakdown voltages vary between the sensors, but this was seen before irradiation as well.

Under forward bias, 5 µm sensors show a similar trend as 50 µm sensors. That is, the forward junction potential increases with irradiation.

CV-curves of the 5 µm sensors were carried out on two different setups. One difference between the setups was the voltage amplitude used for the measurement (250 and 500 mV, at 1 kHz). This fact seems to have impacted results and makes a comparison difficult. Nevertheless, the CV-curves again seem to flatten out with irradiation.

For both thicknesses, it would be interesting to see how the frequency of the CV-measurement affects the results. Due to time limitations, this was not investigated in this project.

3 Transient Current Technique Calibration

The transient current technique (TCT) involves injecting charge at one point on a sensor with a laser pulse and monitoring the resulting signal. Integrating this signal yields the collected charge (in arbitrary units). Thus, TCT can give information about the charge collection efficiency.

This section explains how a TCT setup was calibrated. The goal was to minimize the laser spot size by adjusting laser settings.

3.1 Background

For Gaussian laser beams, the beam width w as a function of axial distance z can be described by

$$w(z) = w_0\sqrt{1+\left(\frac{z-z_0}{z_R}\right)} \quad \text{and} \quad z_R = \frac{\pi w_0^2}{\lambda}, \tag{6}$$

where z_R is the Rayleigh distance, z_0 is the location of waist w_0, and λ is the laser wavelength. This results in the shape in figure 13.

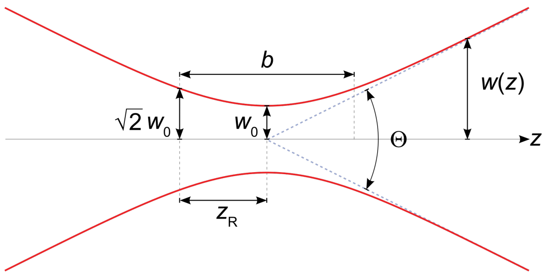

Figure 13: Gaussian beam propagation [3].

The TCT setup is shown in figure 14. It consists of a UV laser (wavelength $\lambda = 375$ nm) exiting an optical fiber (mode field diameter $2 \cdot w = 3.6$ µm. The UV laser is needed to reach the bandgap energy of SiC. A bi-convex lens (focal length $f = 30.0$ mm) then focuses the laser onto a sensor. The laser assembly length and the height z were the parameters to be calibrated.

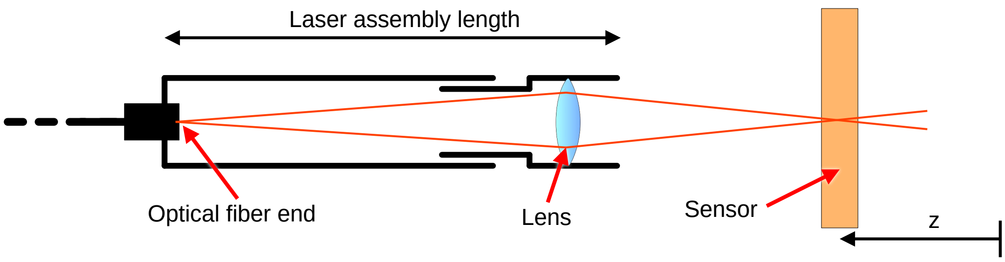

Figure 14: Sketch of the UV TCT laser sysetm.

The optical system in the TCT setup is equivalent to the one in figure 15.

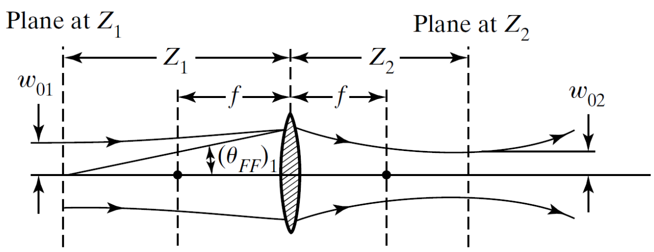

Figure 15: An optical system equivalent to the one used in this project [4].

It can be shown that (see p. 599 in [4]) the parameters in figure 15 are related according to

$$
\begin{aligned}
\frac{1}{w_{02}^2} &= \frac{1}{w_{01}^2}\left(1 - \frac{Z_1}{f}\right)^2 + \frac{1}{f^2}\left(\frac{\pi w_{01}}{\lambda}\right)^2, \\
Z_2 &= f + \frac{f^2(Z_1 - f)}{(Z_1 - f)^2 + (\pi w_{01}^2/\lambda)^2}.
\end{aligned}
\tag{7}
$$

Equation 7 can be used to plot the beam width w_{02} as a function of Z_1, and the distance Z_2 as a function of Z_1. This is shown in figures 16 and 17. Since the goal of this calibration was to minimize w_{02}, large values of Z_1 appear to be best, in theory.

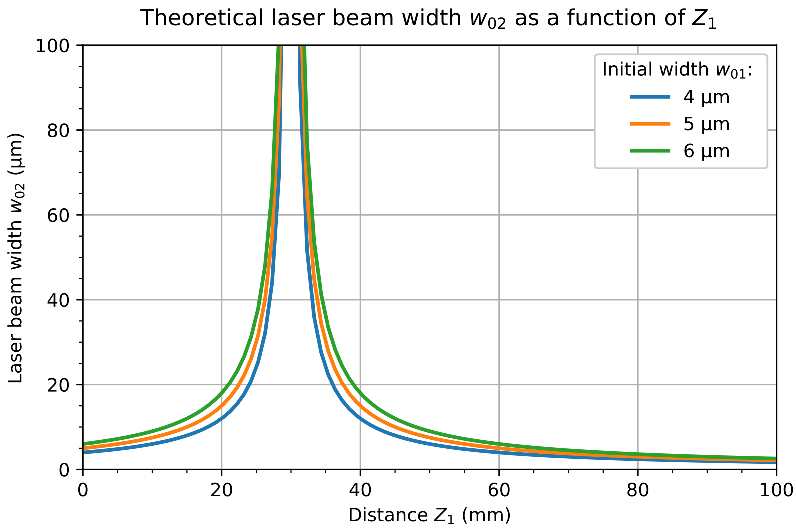

Figure 16: Laser beam width w_{02} as a function of distance Z_1.

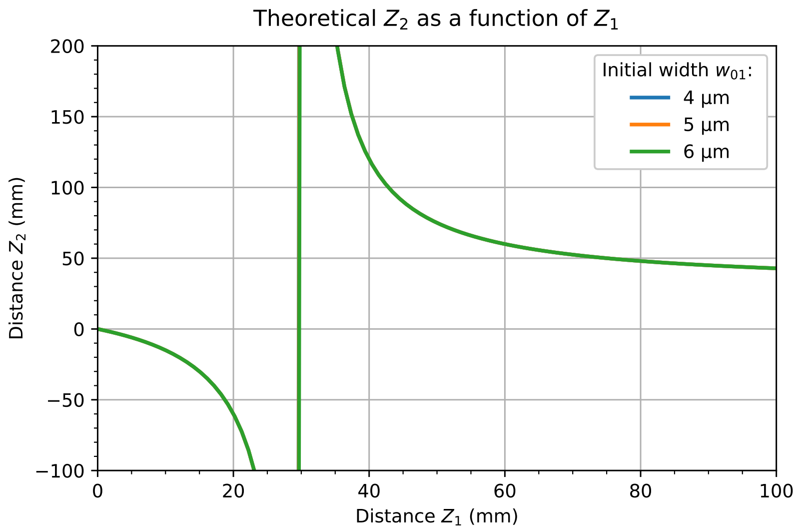

Figure 17: Distance Z_2 as a function of distance Z_1.

3.2 Method

To determine the beam widths, knife-edge scans were performed. This involved moving the (Gaussian) laser beam across an edge and monitoring the collected charge as a function of the laser beam position. This should result in an integral of the Gaussian, which is an error function. If these knife-edge scans are done for different distances to the sensor, one can determine which distance results in the smallest w_0.

First, knife-edge scans on the perimeter of an unirradiated SiC sensor were conducted. The results and entire fitting processes are summarized in appendix D. After that, one knife-edge scan was done on the bond pad of the SiC sensor. This is shown in appendix E. The scan regions of the SiC sensor are shown in figure 18.

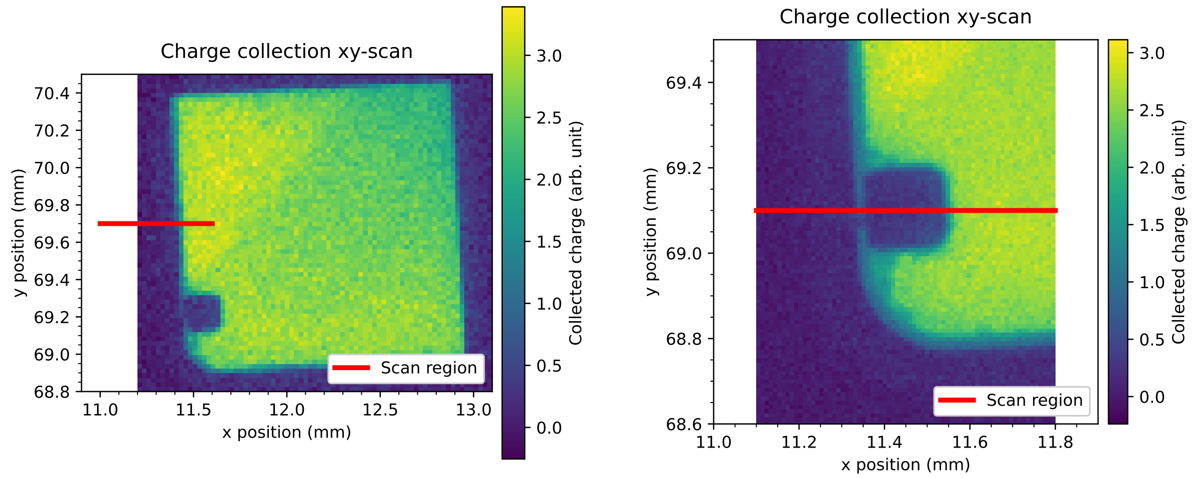

Figure 18: The knife-edge scan region for the SiC sensor perimeter (left) and bond pad (right).

Knife-edge scans were also done on a Si sensor. This was to see if the edges on the SiC sensor were sharp enough to be used for the knife-edge scan. The fitting process is shown in appendix F. The scan region is shown in figure 19.

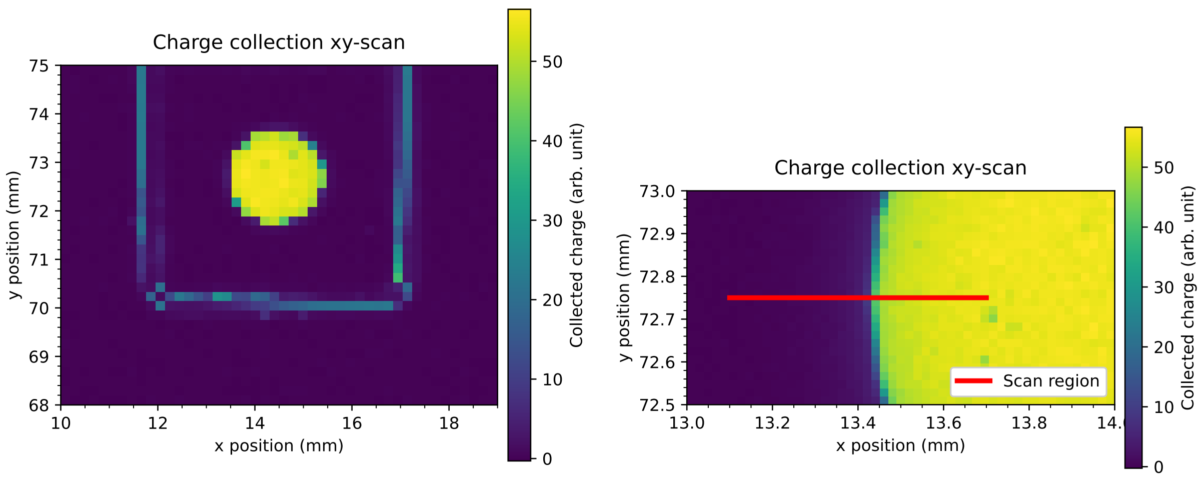

Figure 19: The Si sensor (left) and knife-edge scan region (right).

3.3 Results

The results of the SiC perimeter knife-scan measurements are shown in figure 20. Resulting fit waist sizes w_0 and Rayleigh lengths z_R are presented in figure 21.

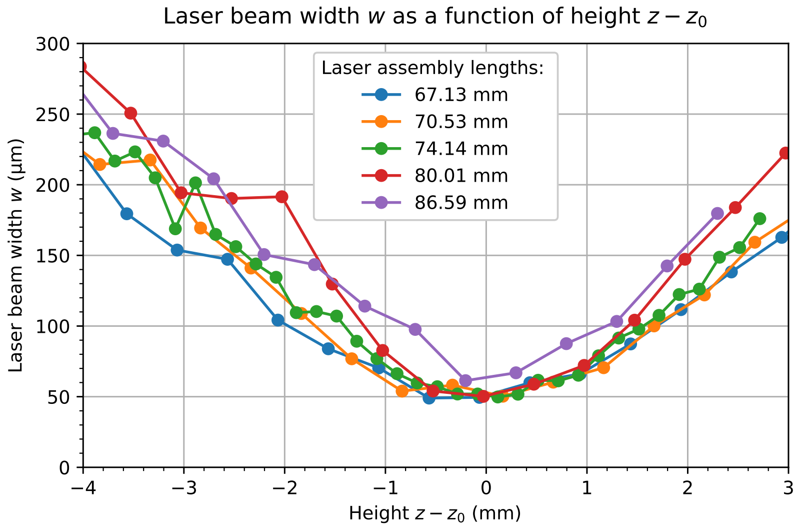

Figure 20: Beam width as a function of axial distance, on SiC sensor perimeter.

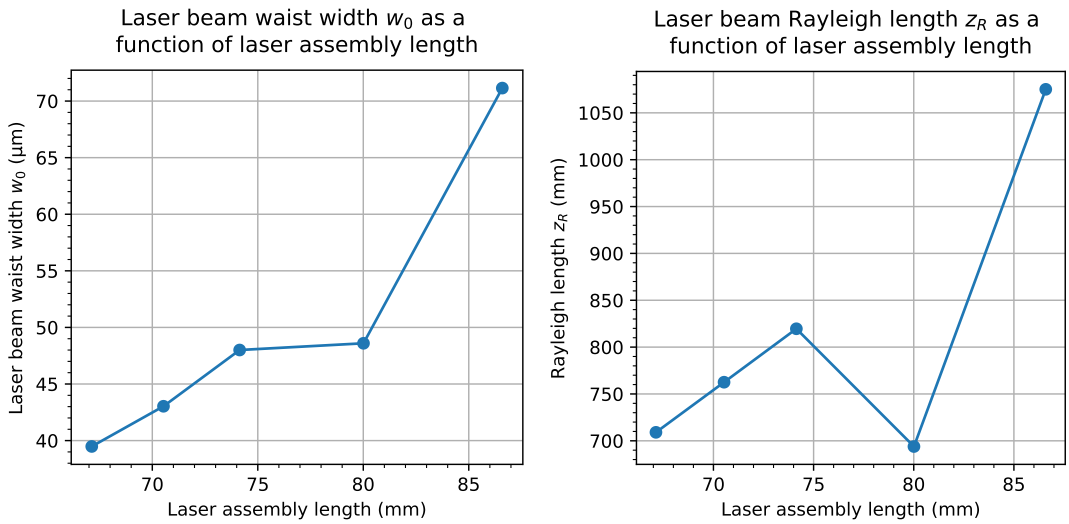

Figure 21: Fit parameters from SiC perimeter scans.

The results of the Si knife-scan measurement are shown in figure 22. Resulting fit waist sizes w_0 and Rayleigh lengths z_R are presented in figure 23.

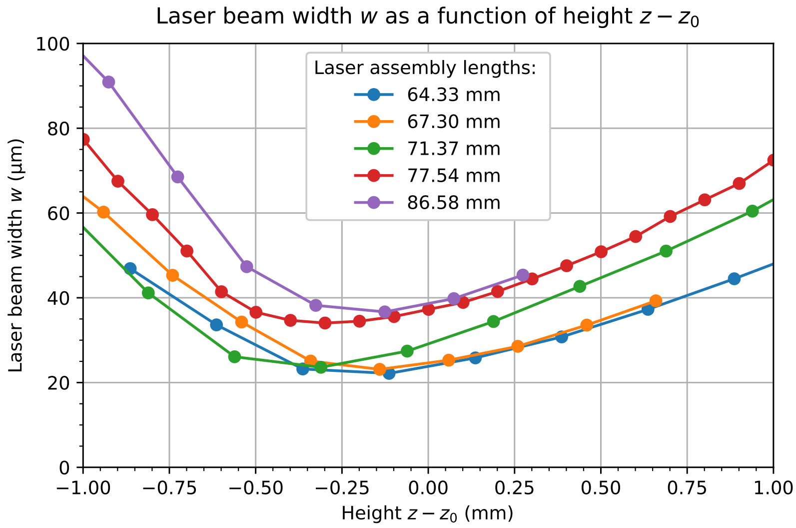

Figure 22: Beam width as a function of axial distance, on Si sensor.

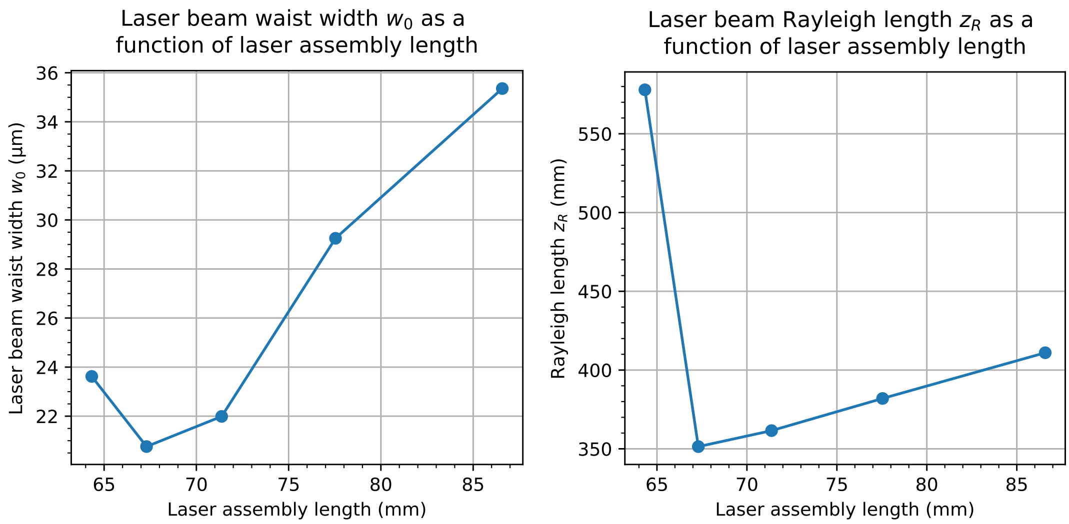

Figure 23: Fit parameters from Si scans.

3.4 Discussion

For the SiC perimeter knife-edge scan, the shapes of the curves in figure 20 look like the expected shapes in figure 13. The fit process in appendix D also looks reasonable. However, the curves in figure 20 do not appear to change with laser assembly lengths. The change that is observed in the fit parameters w_0 and z_R is the opposite of what is expected from figure 16. Both w_0 and z_R should decrease with increasing laser assembly length, in theory. Also, it is remarkable that measured widths w do not go under about 50 µm. These results could indicate that the SiC perimeter edge is not sharp enough and that the fitting process might result is misleading fit parameters. It might also indicate that the laser beam is not Gaussian.

The strange results for the SiC perimeter is the reason for performing the SiC bond pad knife-edge scan. The result of this scan are only shown in appendix E, as they resulted in laser beam widths of about 100 µm. This might indicate that the roughly 200 µm wide bond pad is too small for a knife-edge scan.

The results of the Si knife-edge scan show, similarly to the SiC, a behavior that does not match figure 16. However, the laser beam widths are smaller for these measurements, at about 25 µm. The profile in 22 is not symmetric and some of the error function fits in appendix F do not match well. The reason for this is not known.

In the end, a laser assembly length of 67.33 mm and height z of 27.75 mm was selected moving forward.

4 Transient Current Technique Charge Collection

This section describes how the charge collection efficiency of 50 µm SiC sensors was measured for the unirradiated and irradiated sensors. The results of these measurements are also presented.

4.1 Background

Recall that TCT gives information about charge collection efficiency. For a SiC sensor and a UV laser (375 nm), the charge is liberated along the laser beam in the depleted region. As the depleted region grows with increasing V_{bias} (see appendix C), so does the liberated charge. Neglecting loss of laser intensity, the collected charge as a function of V_{bias} is proportional to the depletion region width W.

4.2 Method

The collected charge was measured for 50 µm SiC sensors as a function of V_{bias}. The measurement for each V_{bias} was taken as the average of 16 measurement positions arranged in a 4-by-4 grid on the SiC sensors. This was done to avoid local fluctuations in charge collection efficiency. For all measurement positions and resulting curves, see appendix G.

The average of the curves was taken between 700-800 V, as the curves were flat in this region. This average value was seen as the charge collection efficiency for the sensor.

The shape of the voltage signal from the sensor was found to vary with the laser beam position on the sensor. Appendix H shows how signals originating close to the bond pad had a larger amplitude (about 120 mV) and were followed by oscillations. The whole signal here was about 10 ns long. Further from the bond pad, signals with a smaller amplitude (about 10 mV) and a length of about 40 ns were observed.

Charge collection efficiency was found to change with temperature. This is shown in appendix I. Between -20 °C and 20 °C, SiC was found to have a temperature coefficient of about 1.65 %/°C.

To assess the effect of the choice of the 4-by-4 measurement grid position, a study was made for different positions on the same sensor, for two different unirradiated sensors. This is shown in appendix J. The results indicate a small variation, as long as all 16 points are roughly in the same region of the sensor. Thus, the measurements are seen as representative of each respective sensor.

Recall that the 10^{15} p/cm^2 sensor could reach a high forward voltage before reaching the forward junction potential. The signals produced by biasing the 10^{15} p/cm^2 sensor with different voltages are shown in appendix K, including a forward bias of 400 V. The results indicate that the pulses look the same but with opposite polarities.

4.3 Results

The collected charge as a function of bias voltage for the different sensors is shown in figure 24. The average charge collection efficiency between 700-800 V is shown in figure 25. In this figure, the charge collection efficiency has been normalized to the mean of the two measurements that were performed on unirradiated sensors.

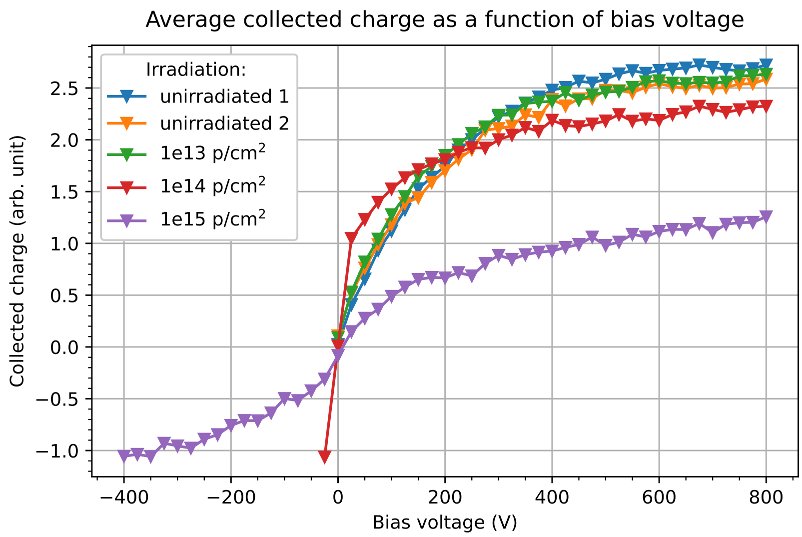

Figure 24: Charge collection efficiency as a function of bias voltage for 50 µm SiC sensors.

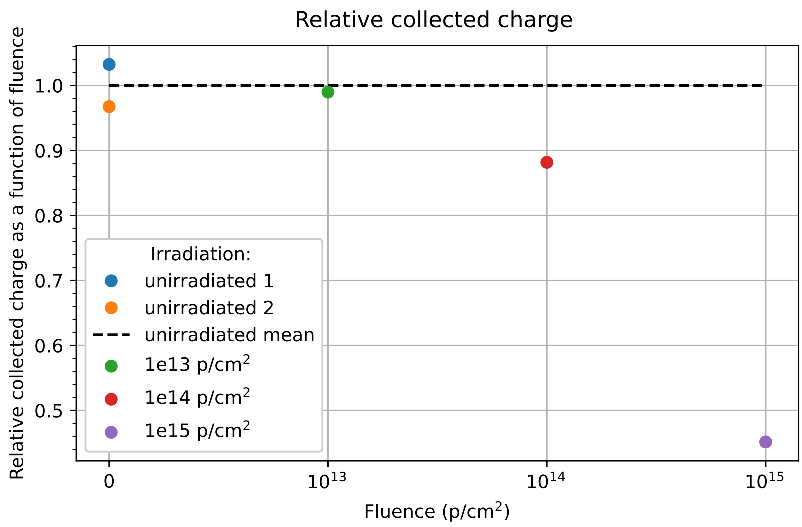

Figure 25: Charge collection efficiency for unirradiated and proton irradiated 50 µm SiC sensors.

4.4 Discussion

The results show a decreasing charge collection efficiency with increasing fluence. The 10^{15} p/cm^2 sensor has about half of the charge collection efficiency of unirradiated sensors. The 10^{14} p/cm^2 sensor is about at 90% of the unirradiated sensors.

The charge collection curves as a function of V_{bias} also appear to follow the W curves in appendix C.

The charge collection efficiency was found to vary between the two unirradiated SiC sensors. This variation was larger than the difference to the 10^{13} p/cm^2 sensor. This indicates that there is some uncertainty in the results. By measuring the same sensors before and after irradiation, one could counteract this.

Due to time limitations, only 50 µm sensors were mentioned in this report. However, preliminary measurements performed for 5 µm sensors indicate almost no difference in charge collection efficiency between unirradiated and irradiated sensors.

5 Conclusions

This section summarizes some of the main conclusions from this project.

For IV-measurements, no change was observed for the reverse bias properties of proton irradiated SiC sensors. However, measurements with higher reverse bias voltages (>1000 V) and better current resolution (<1 pA) would be needed to be certain. The forward junction potential of proton irradiated SiC sensors increases with fluence. For 50 µm thick unirradiated sensors, it was about 1.8 V, but for the 10^{15} p/cm^2 sensor it was above 400 V.

For both 5 µm and 50 µm thick sensors, CV-curves flatten out for irradiated sensors.

The curves appear flat above 10^{14} p/cm^2. This indicates that diode properties are lost. Also, for lower fluences of 10^{13} p/cm^2, the depletion voltage decreases and the effective doping concentration decreases.

The UV TCT setup successfully was able to measure beam widths as a function of axial distance for the SiC sensors. These curves match the expected shapes. Beam widths of down to 25 µm were obtained. However, changing the laser assembly length did not result in the expected behavior. This could indicate that the laser beam is not Gaussian and that some parts of the optical setup are less than ideal. Results indicate that there is a difference between the edge used for the knife-edge scans.

The UV TCT charge collection results show that charge collection efficiency decreases with increased proton fluence and irradiation. At 10^{15} p/cm^2, charge collection efficiency was about half of the unirradiated sensor's value.

Due to time limitations, charge collection results for 5 µm sensors were not included in this report. Furthermore, no defect spectroscopy results were included. Defect spectroscopy is, at the time of writing, ongoing for the SiC sensors. Because of the time limitations, some details of measurement setups and conditions were also omitted in this report.

References

[1] Marzio De Napoli. SiC detectors: A review on the use of silicon carbide as radiation detection material. *Frontiers in Physics*, 2022. doi:10.3389/fphy.2022.898833.

[2] S. M. Sze and Kwok K. NG. *Physics of Semiconductor Devices*. Wiley, 3rd edition, 2007.

[3] Wikimedia Commons. File:GaussianBeamWaist.svg. URL: https://commons.wikimedia.org/wiki/File:GaussianBeamWaist.svg.

[4] Frank L. Pedrotti, Leno M. Pedrotti, and Leno S. Pedrotti. *Introduction to Optics*. Pearson Education, 3rd edition, 2006.

A All Current-Voltage Measurements

This appendix presents all measured IV-curves for unirradiated sensors. Figure 26 and 27 show 50 and 5 µm thick sensors, respectively. Most sensors have similar break-down voltages (>1000 V for 50 µm, ≈120 V for 5 µm). However, some sensors were found to deviate from these values. Moreover, a couple sensors were measured to have a very high current and were deemed to be defective.

Forward bias measurements are more consistent between sensors. Both thicknesses had built-in potentials of approximately 1.8 V. Forward bias measurements were not performed for all sensors, as some had been sent to irradiation already.

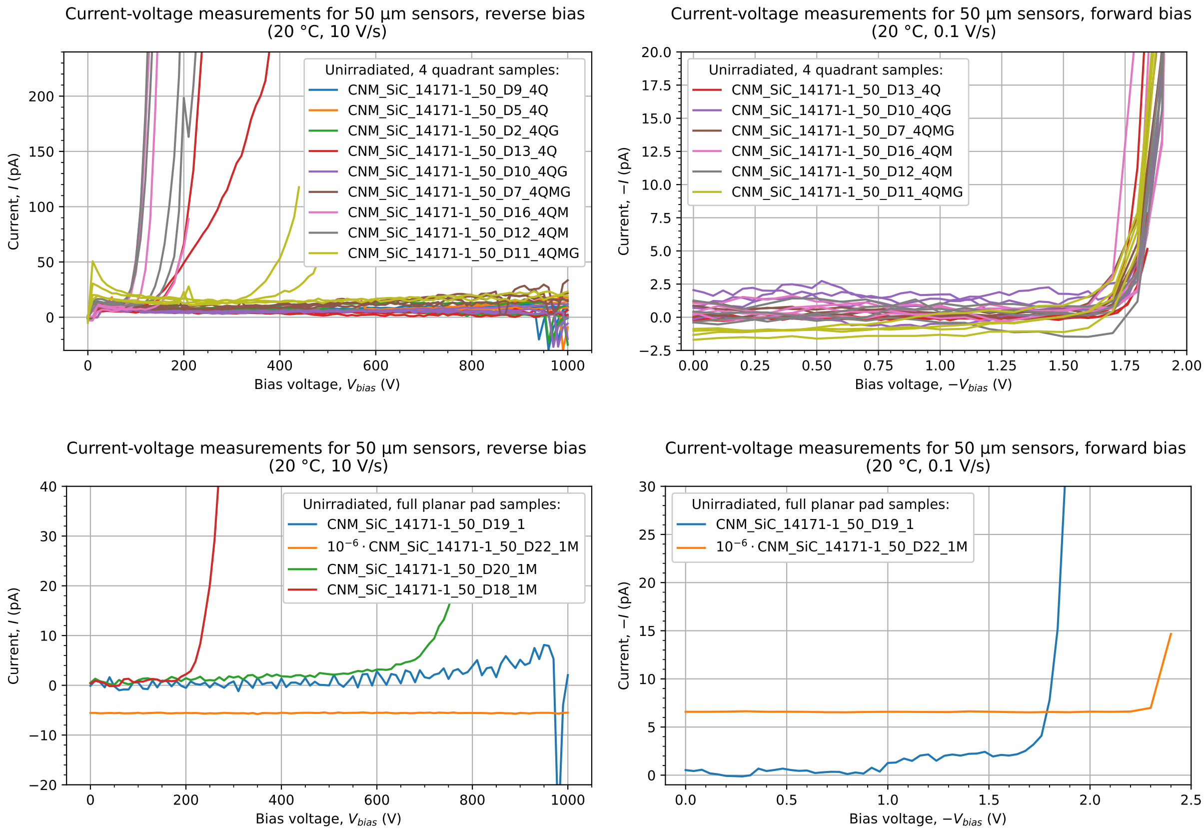

Figure 26: All measured IV-curves for 50 µm thick sensors. Sensor D22 was deemed defective.

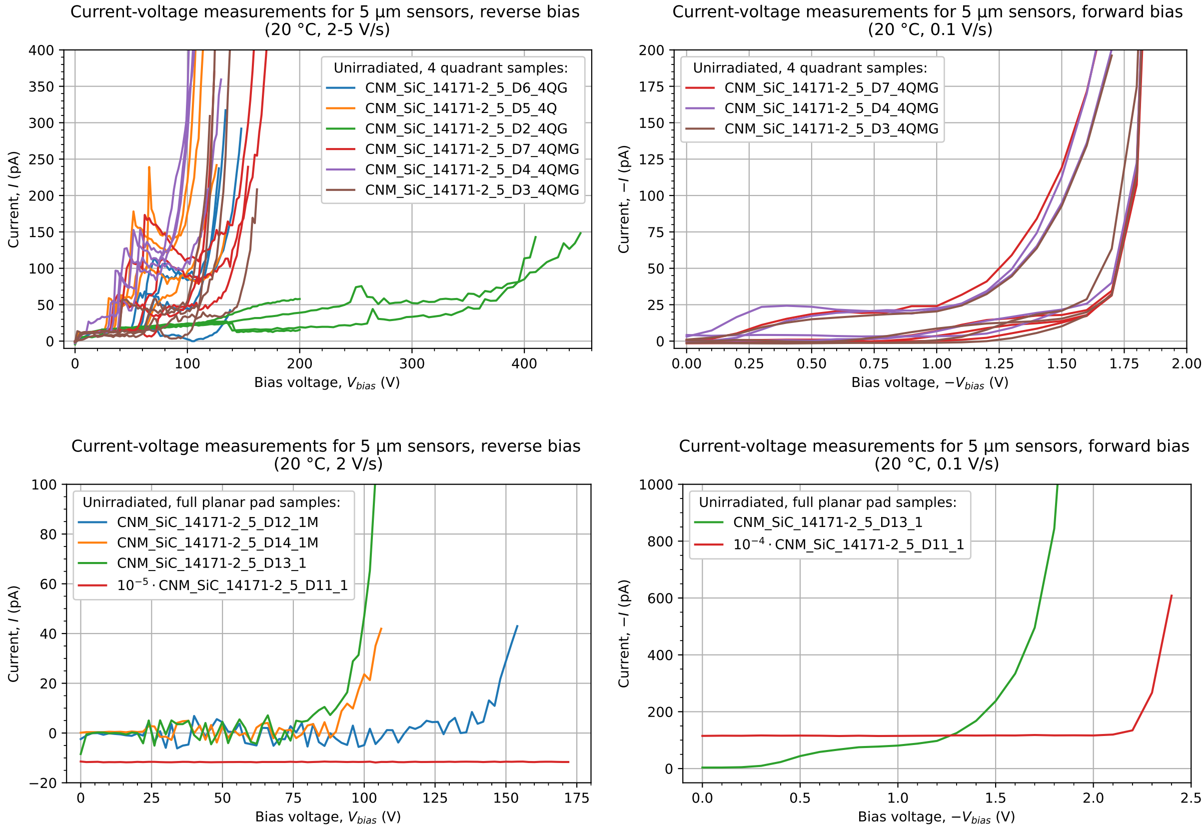

Figure 27: All measured IV-curves for 5 µm thick sensors. Sensor D11 was deemed defective.

B Current-Voltage Ramping Speeds

This appendix shows IV-curves for different ramping speeds in figure 28. Slow ramping speeds (0.1 V/s) are required to measure leakage currents. For higher ramping speeds, an elevated current is measured. The reason for this was not determined. Temperatures of 20 °C and -20 °C do not appear to make a difference. Ramping the voltage up or down does not appear to make a difference, although in two cases there are bumps ramping up below 200 V. The reason for this was not determined.

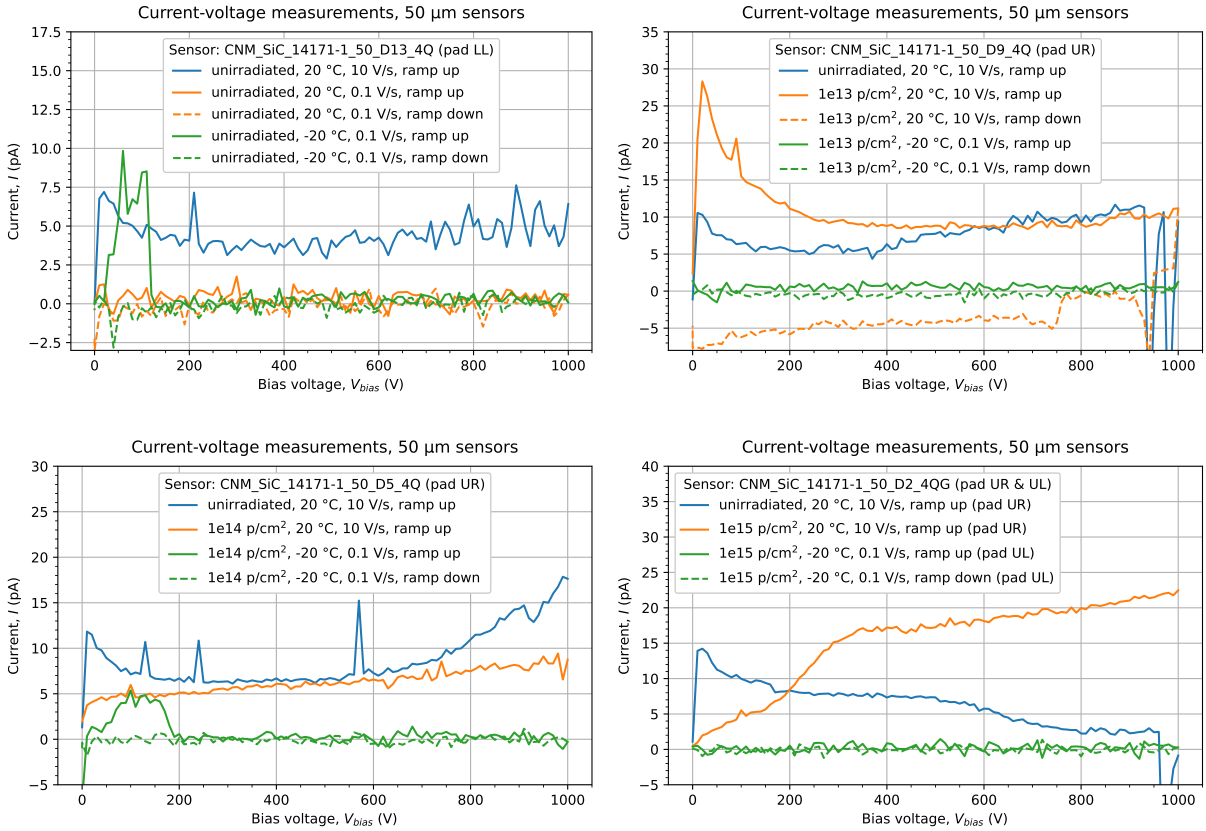

Figure 28: IV-curves for different sensors and with different ramping speeds.

C Typical Capacitance-Voltage Characteristics

This appendix shows the CV-characteristics for typical 50 and 5 µm thick sensors in figure 29 and 30, respectively. All measured sensors of the same thickness and area had similar CV-characteristics. The depletion region width as a function of bias voltage is shown in the figures. $1/C^2$-plots are also presented along with estimated depletion voltages, V_{dep}, and estimated effective doping concentrations from the slope, $N_{eff,s}$, and from the kink (from V_{dep}), $N_{eff,k}$.

For the 50 µm sensors, the estimated N_{eff} matches the manufacturer's specification of $2 \cdot 10^{14}$ cm^{-3}. The depletion width is between 40-50 µm.

For the 5 µm sensors, the width is greater than 5 µm for very low voltages. This means that the sensors are nearly depleted at 0 V and that the $1/C^2$-plot does not look as expected.

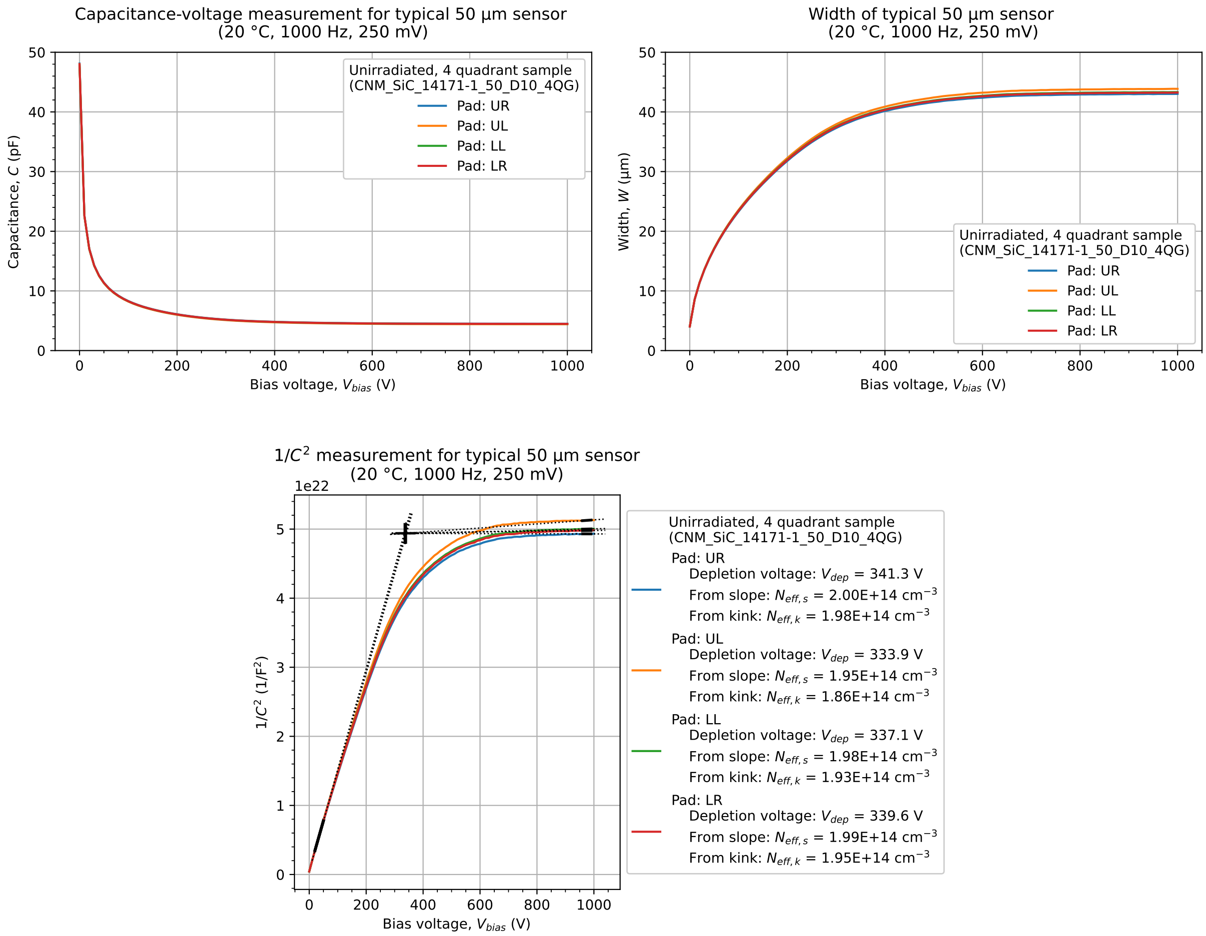

Figure 29: CV-curve, depletion width, and $1/C^2$-plot for a typical 50 µm thick sensor.

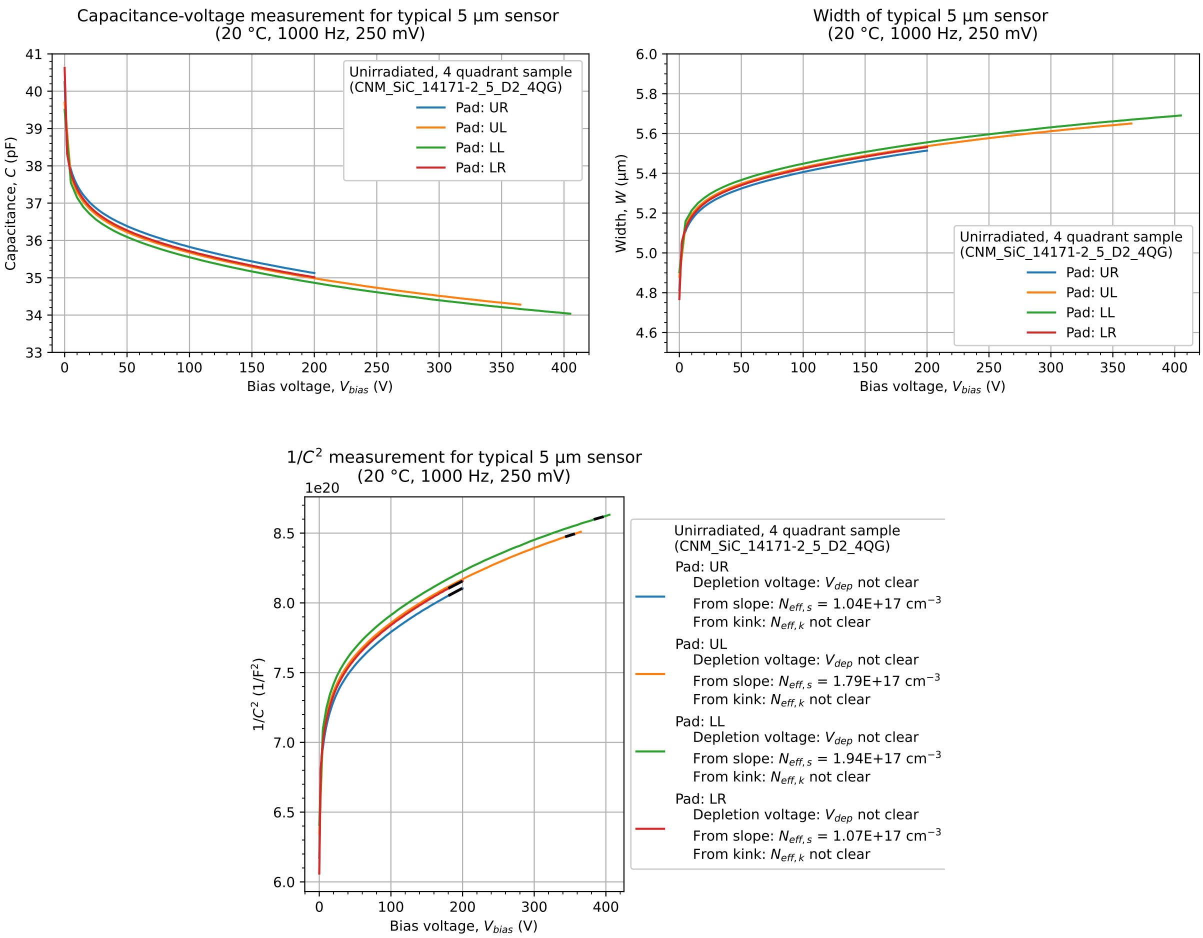

Figure 30: CV-curve, depletion width, and $1/C^2$-plot for a typical 5 µm thick sensor.

D Knife-Edge Scan on SiC Sensor Perimeter

This appendix consists of all knife-edge scan measurements that were performed on the SiC sensor perimeter. Each measurement is for a different laser assembly length (67.13, 70.53, 74.14, 80.01, or 86.59 mm). The scans are shown in figures 31-35.

Each figure presents the collected charge as a function of position x across the edge, with and without fit error functions, for different height positions z. The width of the laser beam is calculated from the fit parameters. Another fit is performed on the laser beam widths to obtain the waist width w_0, waist position z_0, and Rayleigh length z_R.

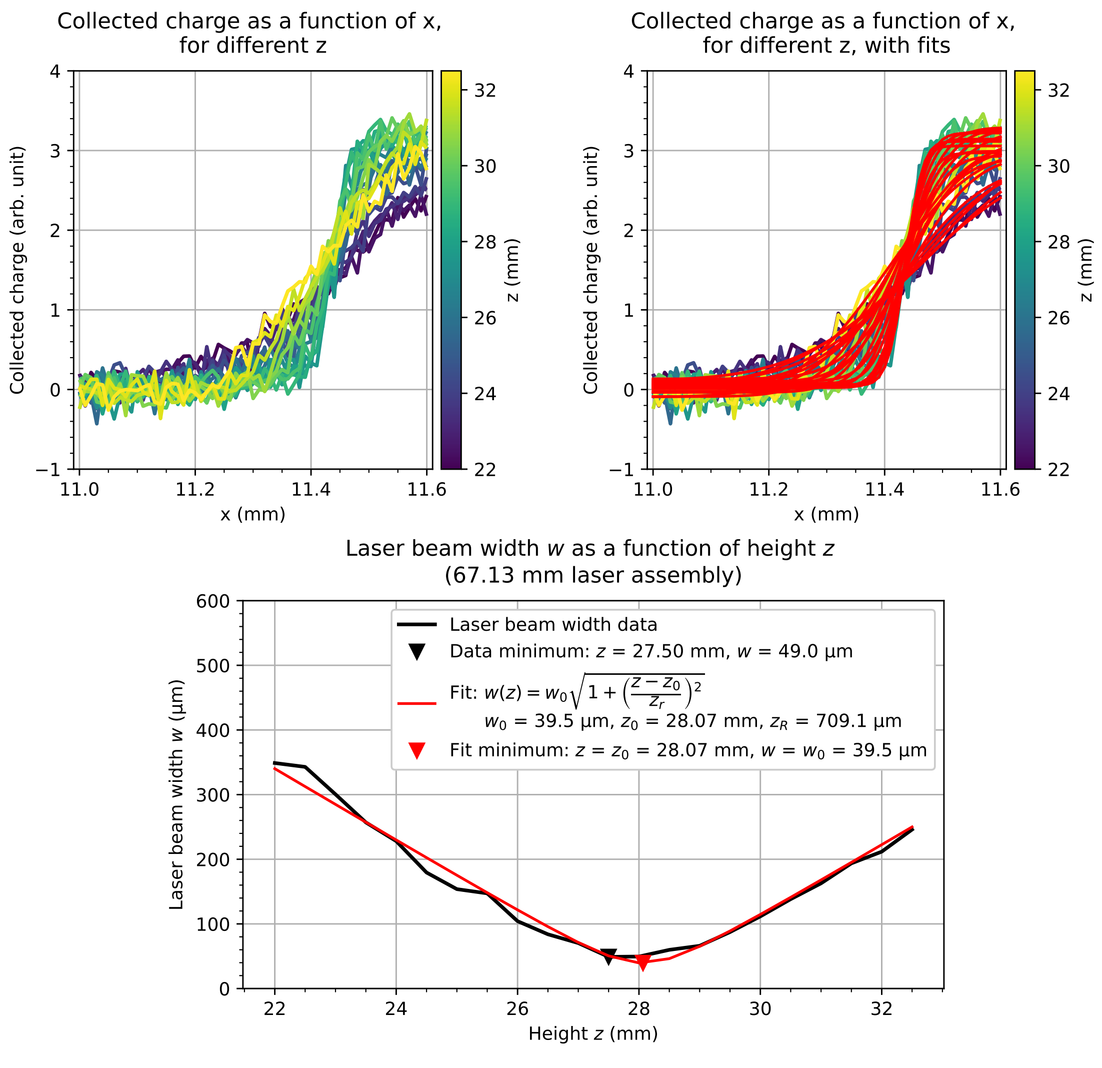

Figure 31: SiC perimeter knife-edge scan for a laser assembly length of 67.13 mm.

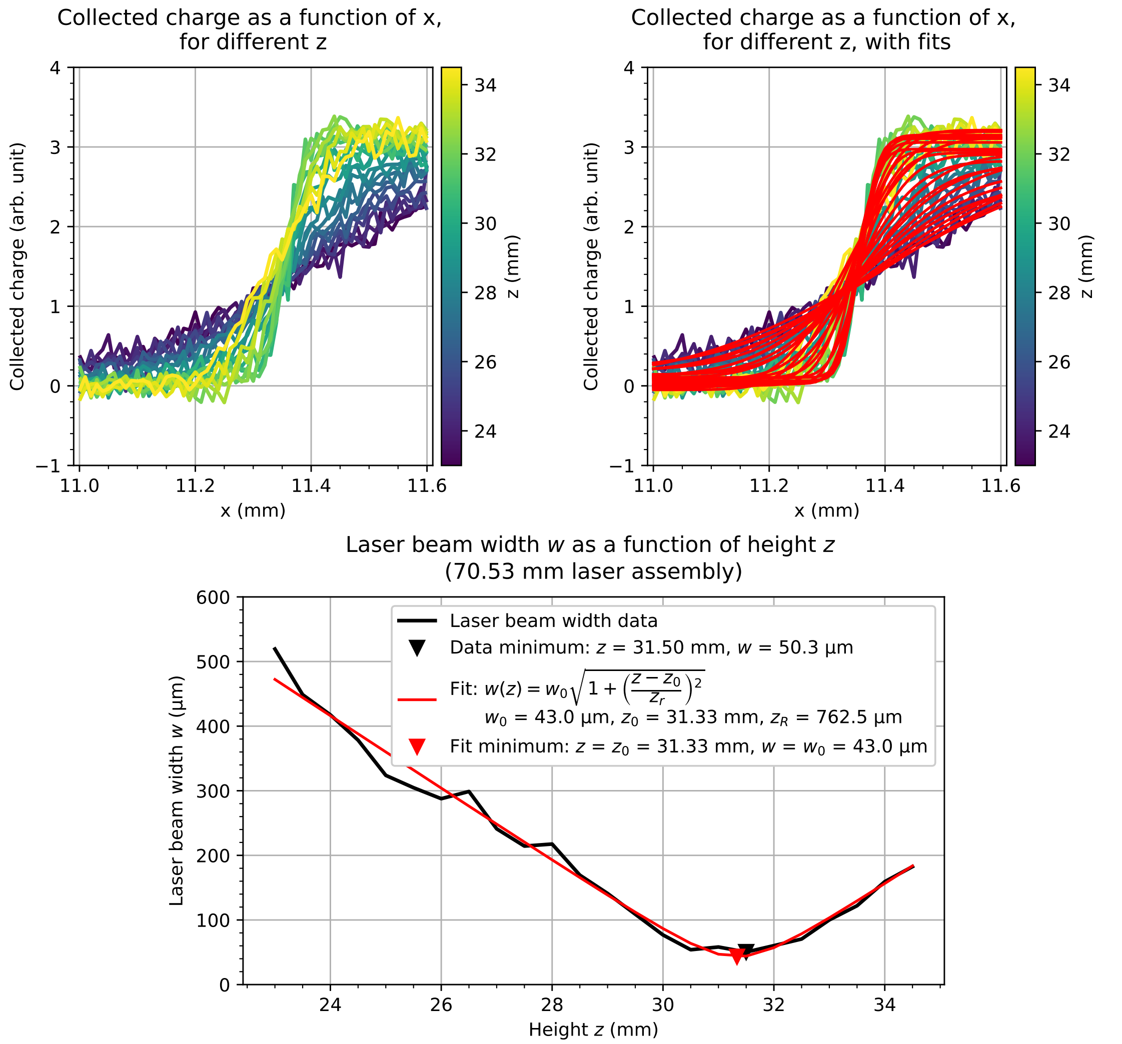

Figure 32: SiC perimeter knife-edge scan for a laser assembly length of 70.53 mm.

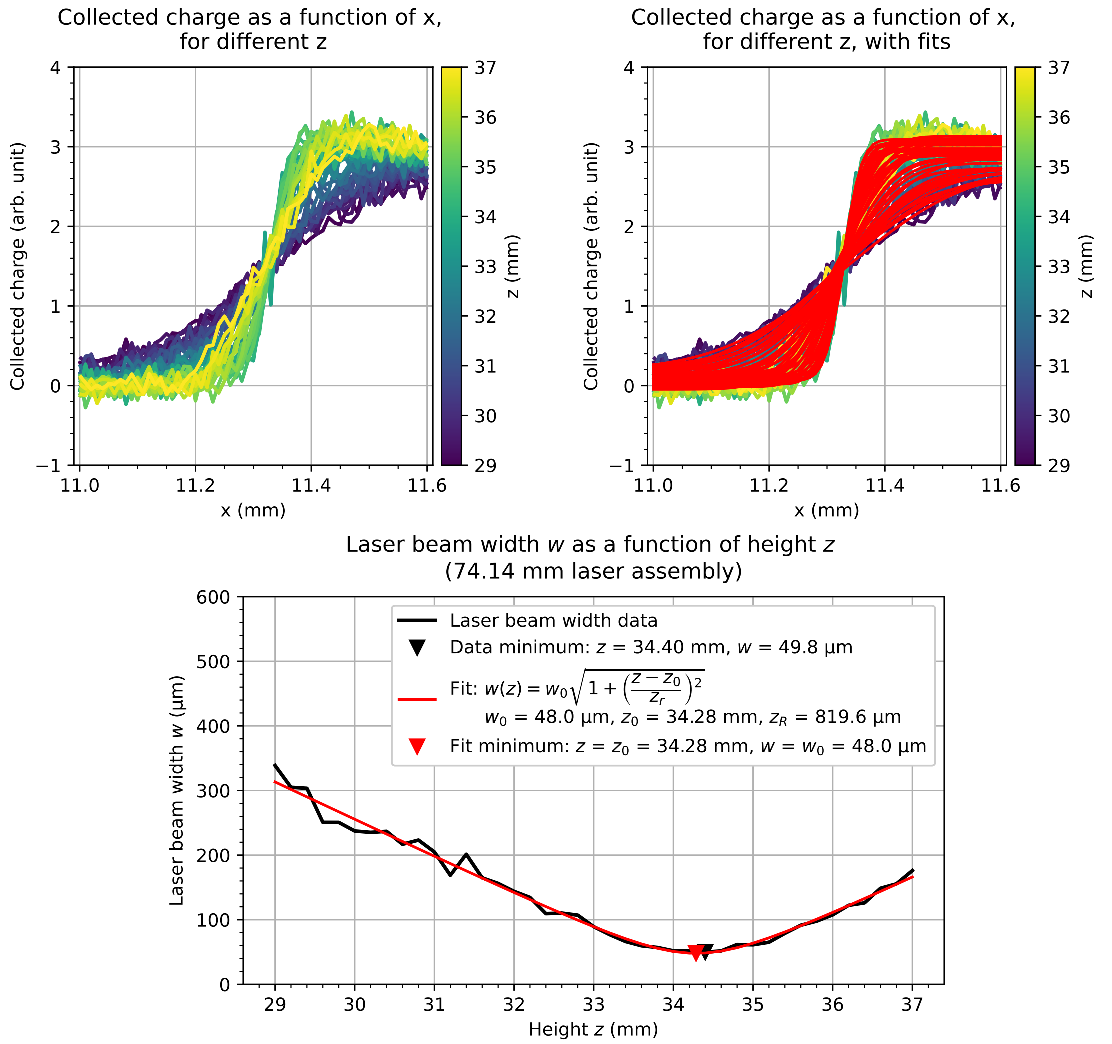

Figure 33: SiC perimeter knife-edge scan for a laser assembly length of 74.14 mm.

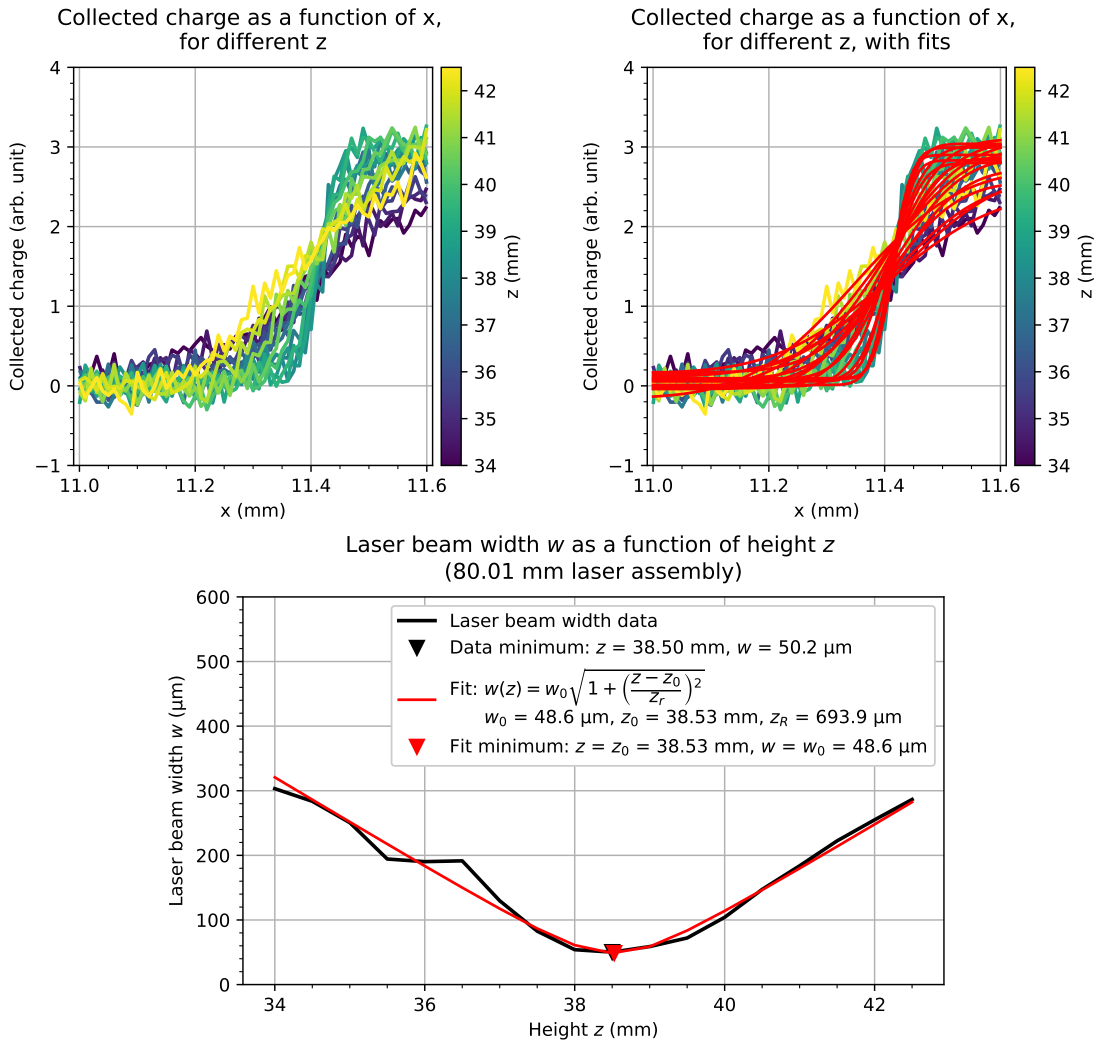

Figure 34: SiC perimeter knife-edge scan for a laser assembly length of 80.01 mm.

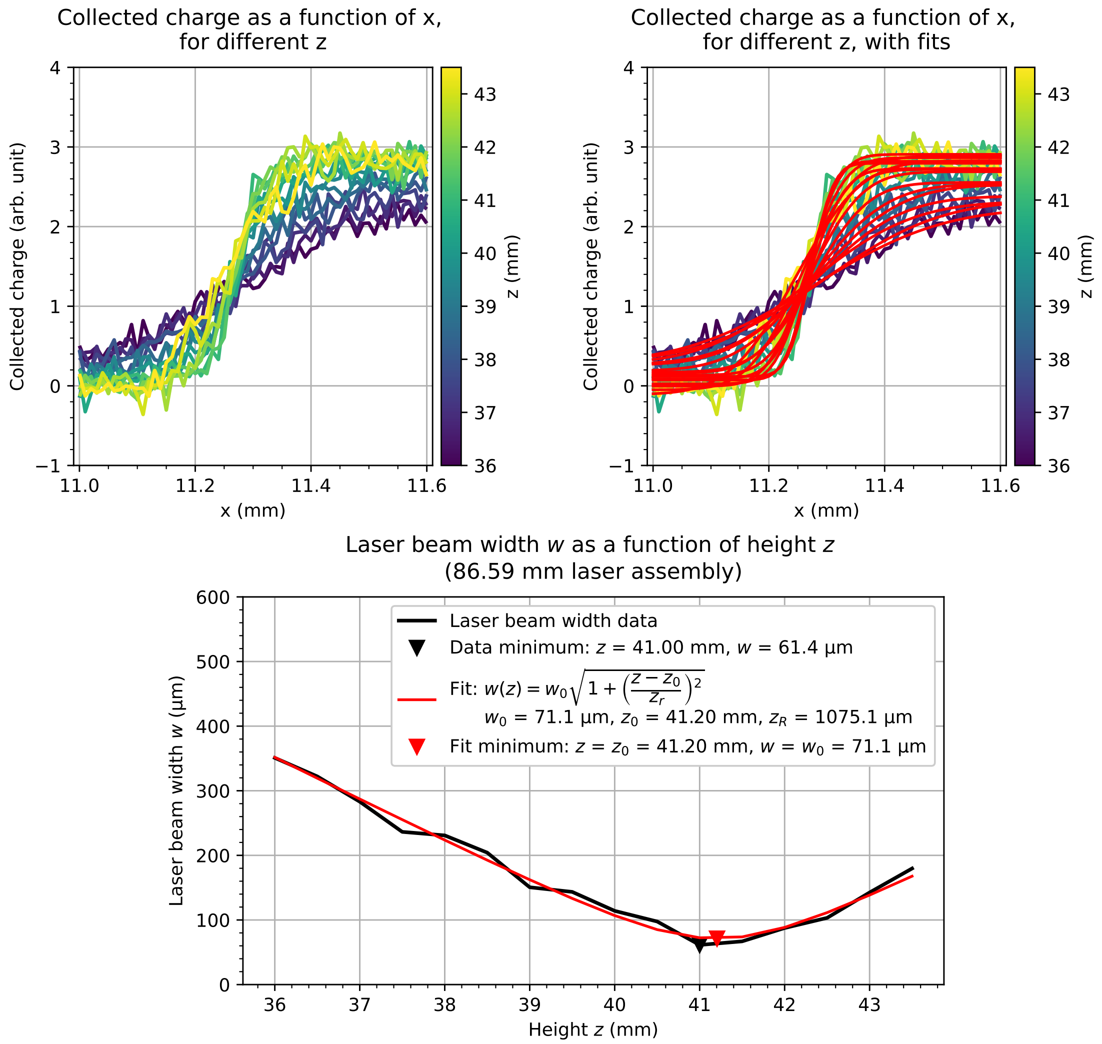

Figure 35: SiC perimeter knife-edge scan for a laser assembly length of 86.59 mm.

E Knife-Edge Scan on SiC Sensor Bond Pad

This appendix consists of the knife-edge scan measurement that was performed on the SiC sensor bond pad. The measurement is for a laser assembly length of 67.30 and is shown in figure 36.

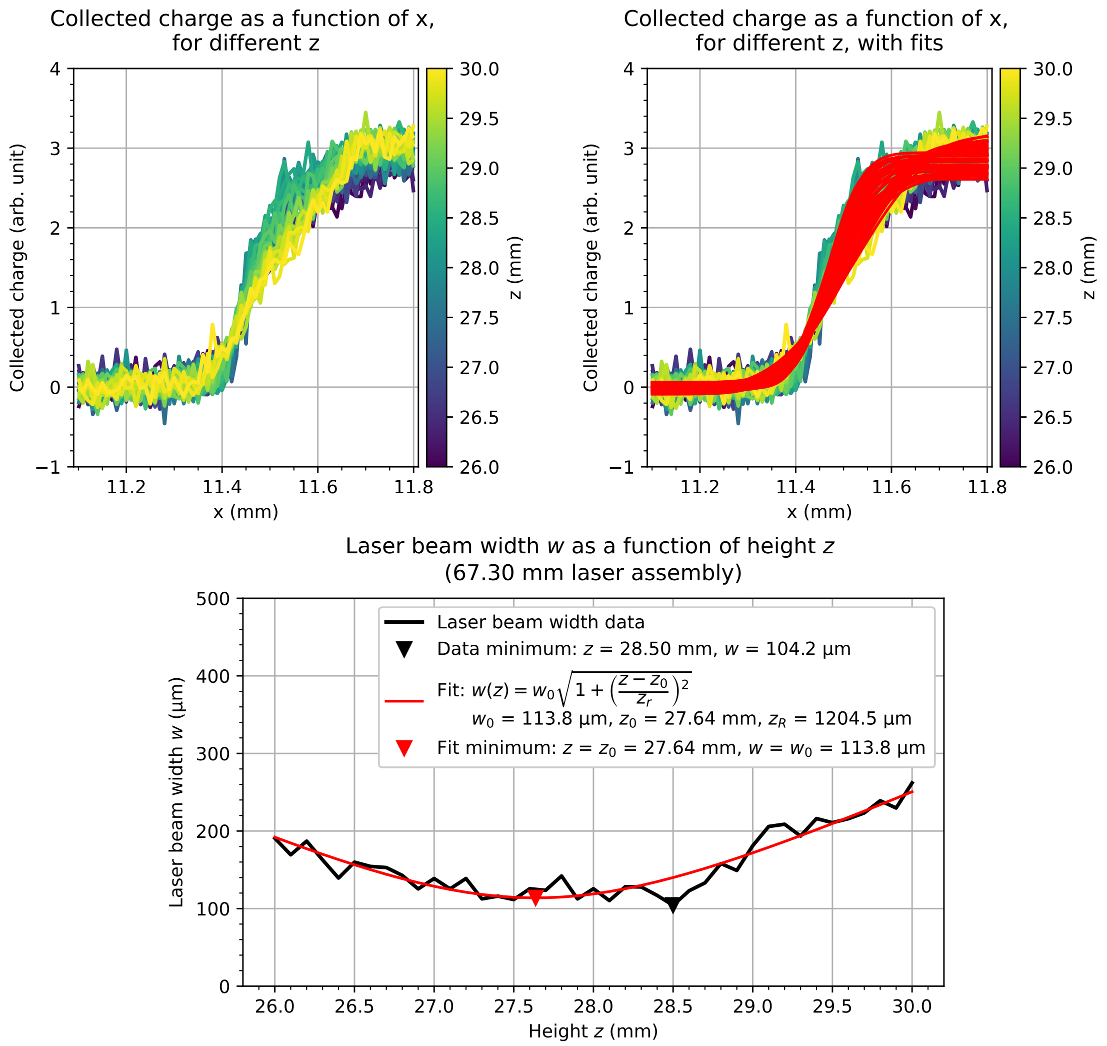

Figure 36: SiC bond pad knife-edge scan for a laser assembly length of 67.30 mm.

F Knife-Edge Scan on Si Sensor

This appendix consists of all knife-edge scan measurements that were performed on the Si sensor. Each measurement is for a different laser assembly length (64.33, 67.30, 71.37, 77.54, or 86.58 mm). The scans are shown in figures 37-41.

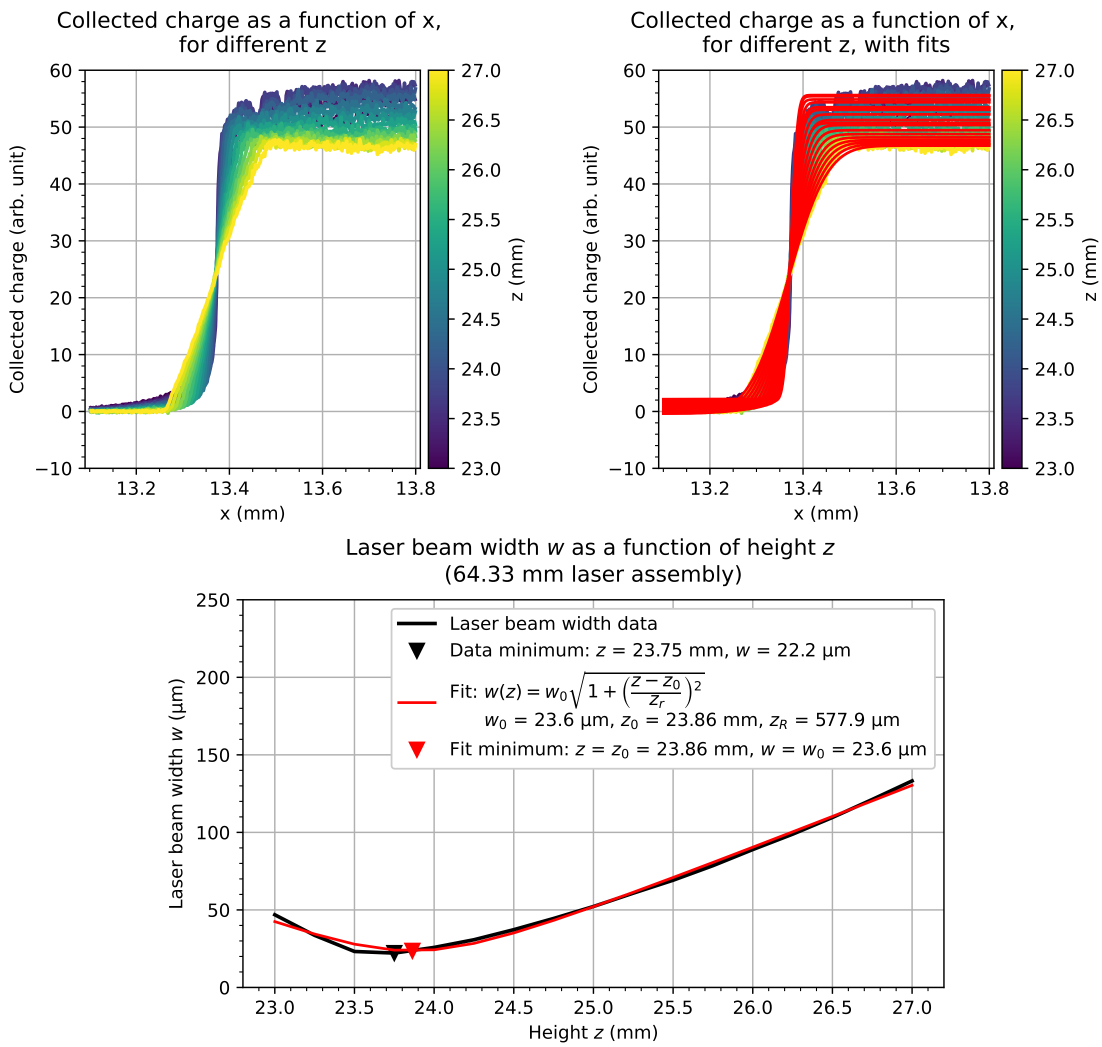

Figure 37: Si knife-edge scan for a laser assembly length of 64.33 mm.

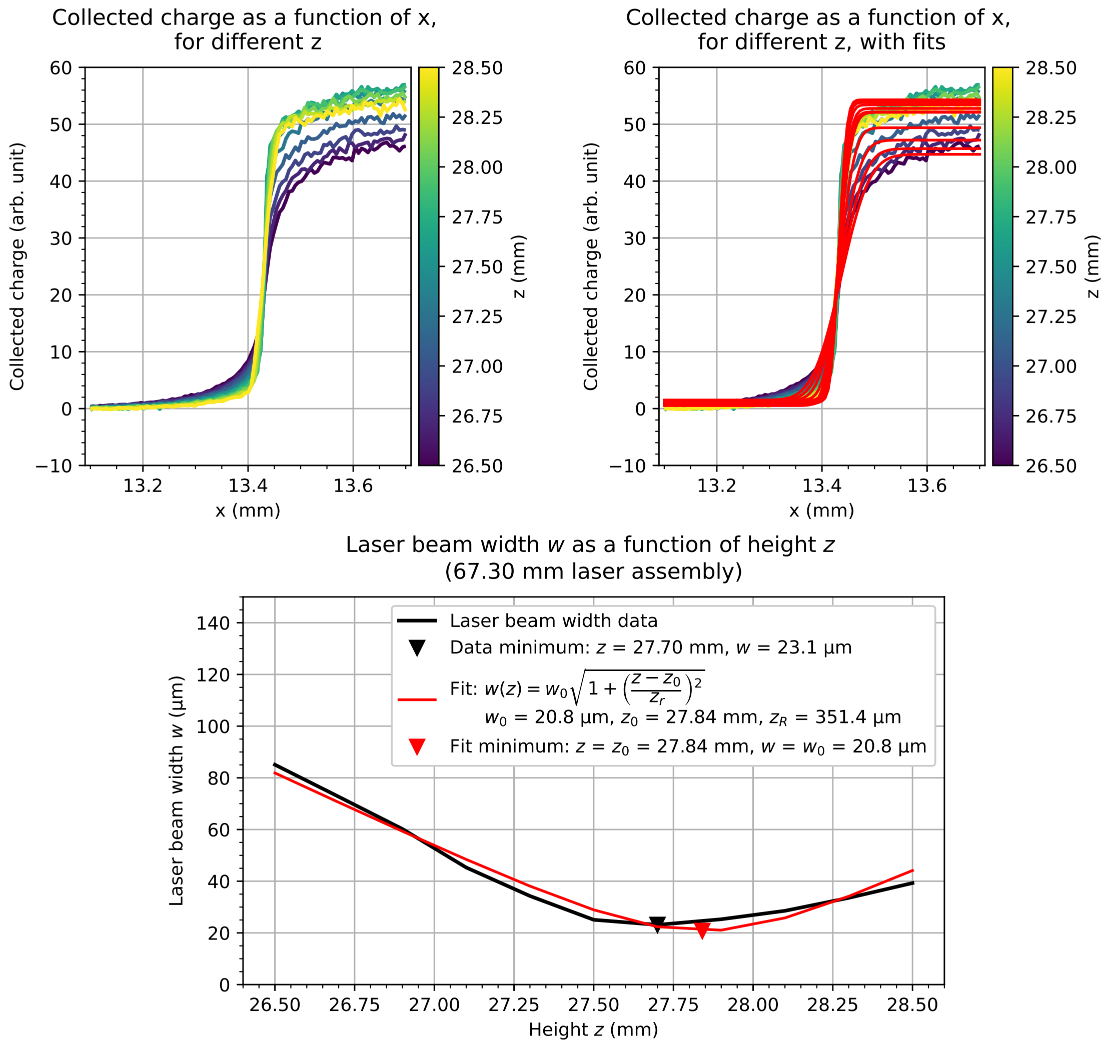

Figure 38: Si knife-edge scan for a laser assembly length of 67.30 mm.

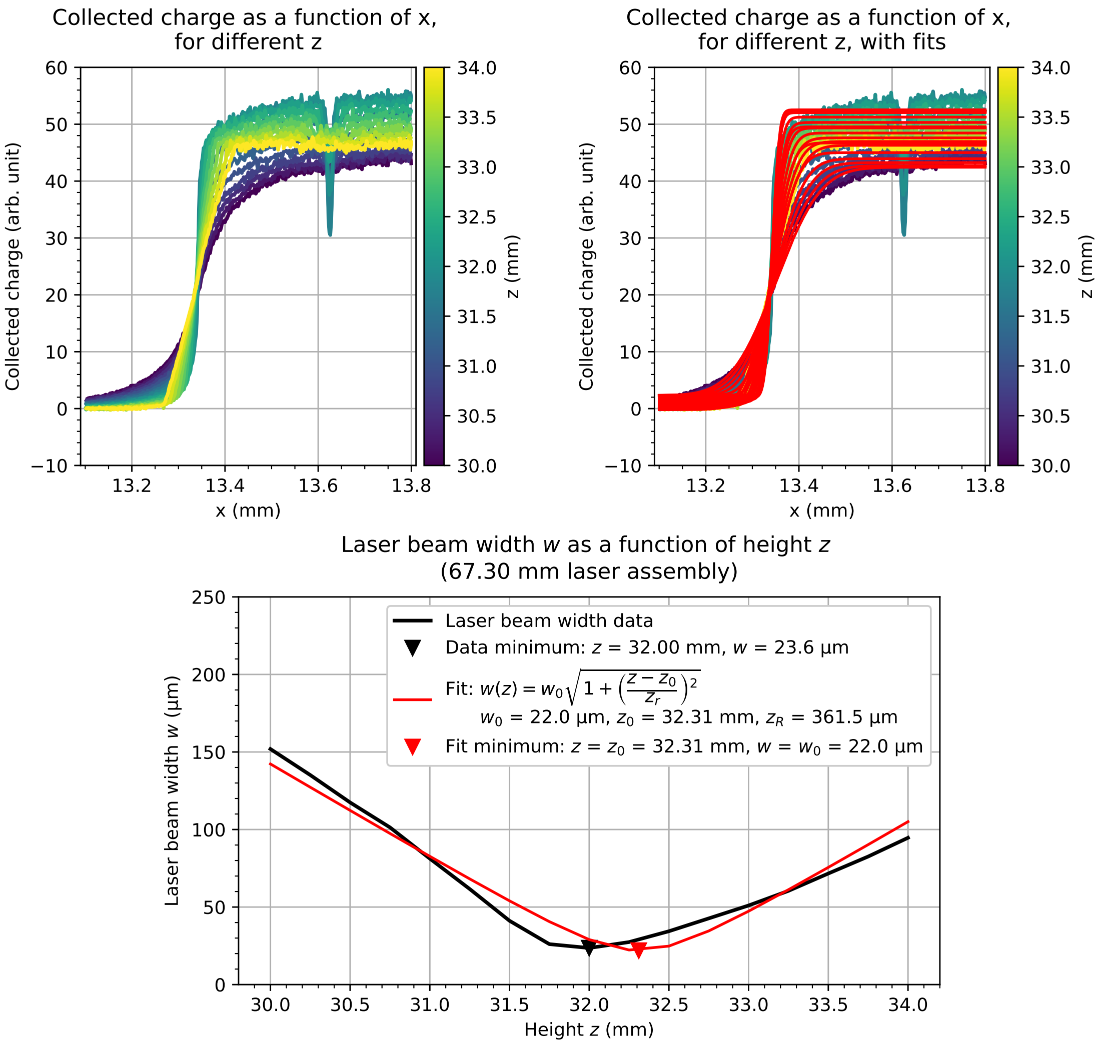

Figure 39: Si knife-edge scan for a laser assembly length of 71.37 mm.

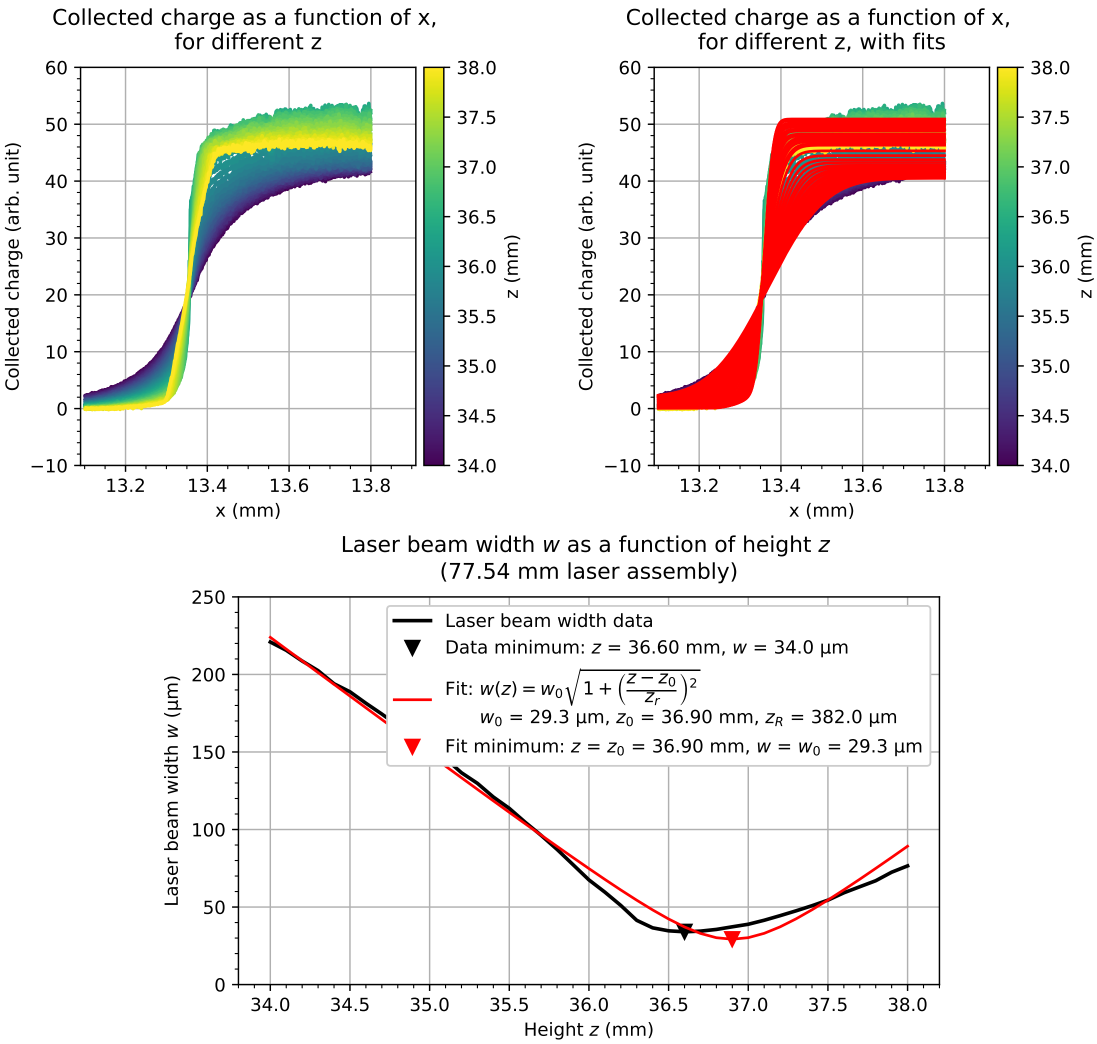

Figure 40: Si knife-edge scan for a laser assembly length of 77.54 mm.

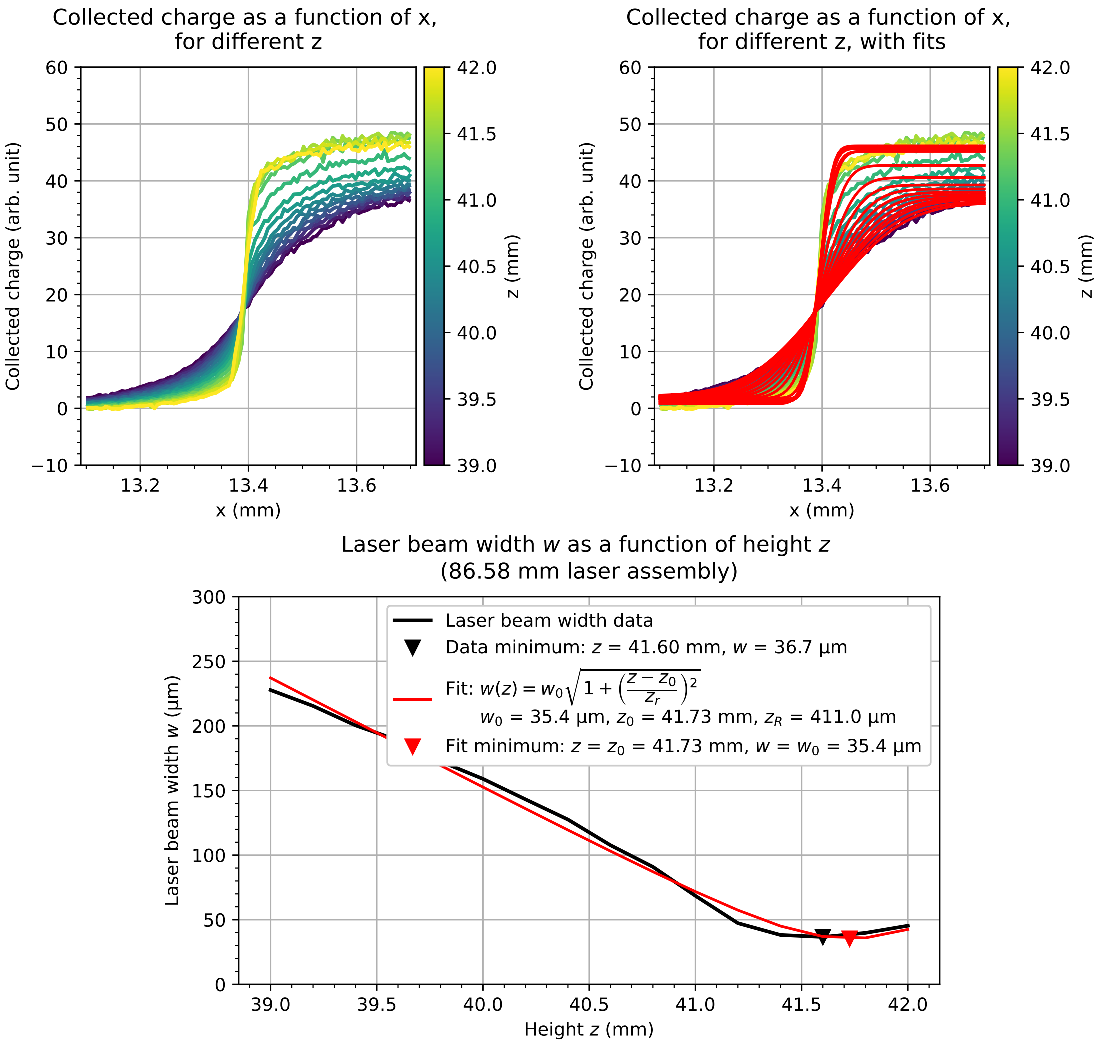

Figure 41: Si knife-edge scan for a laser assembly length of 86.58 mm.

G Charge Collection Measurements

This appendix shows the charge collection measurements that were performed on 50 µm sensors. The plots show measurement positions and average charge collection between the measurement positions as a function of bias voltage, in figures 42-46.

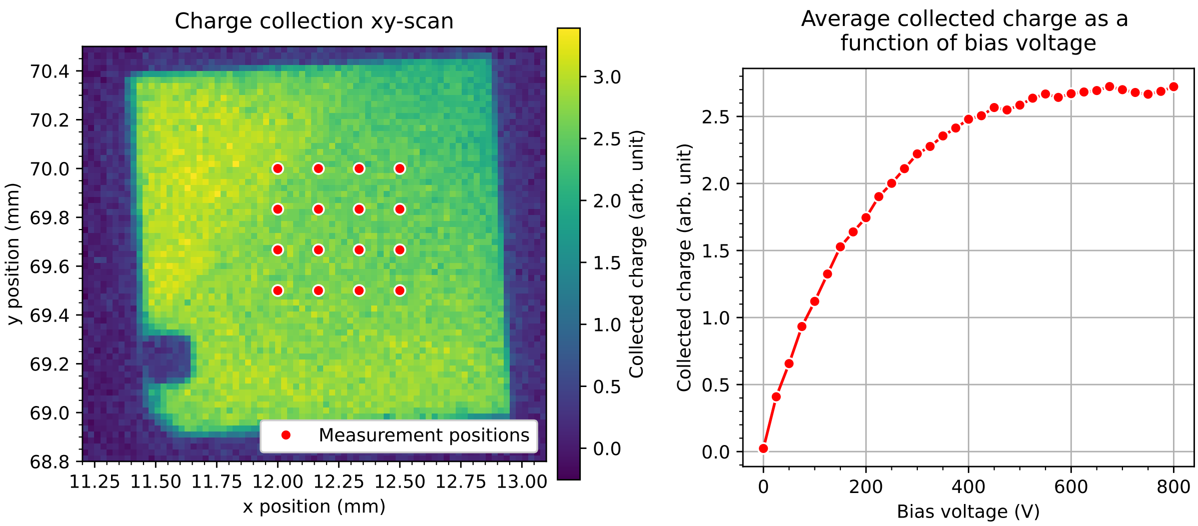

Figure 42: Unirradiated sensor 1, with measurement positions and collected charge at different bias voltages.

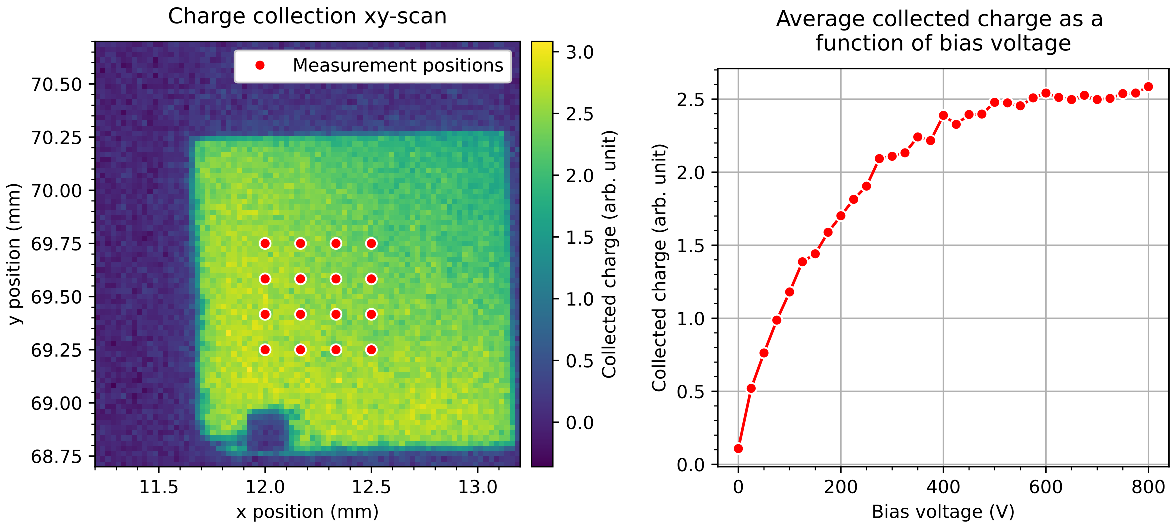

Figure 43: Unirradiated sensor 2, with measurement positions and collected charge at different bias voltages.

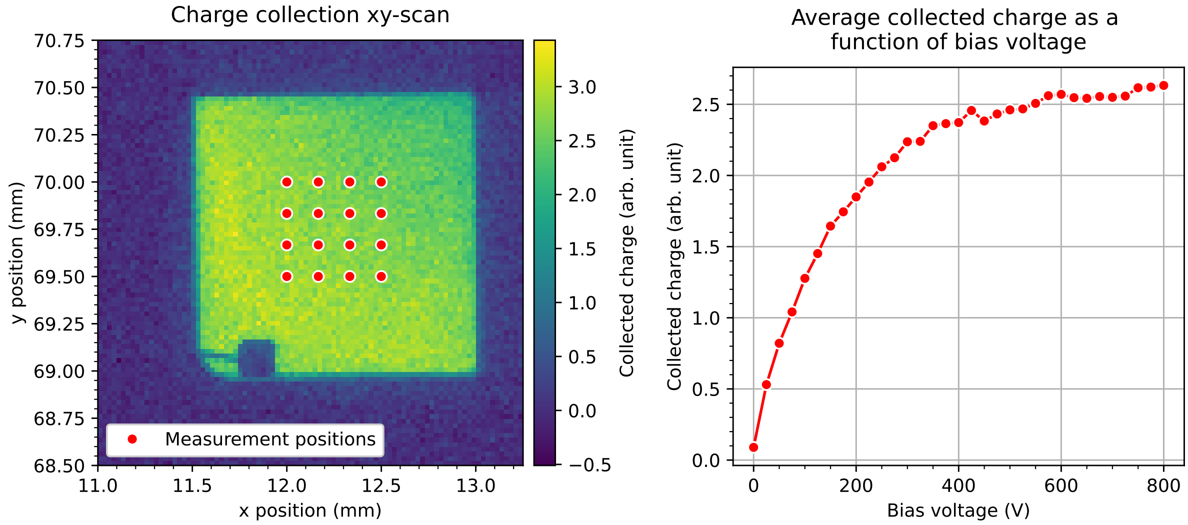

Figure 44: 10^{13} p/cm^2 sensor, with measurement positions and collected charge at different bias voltages.

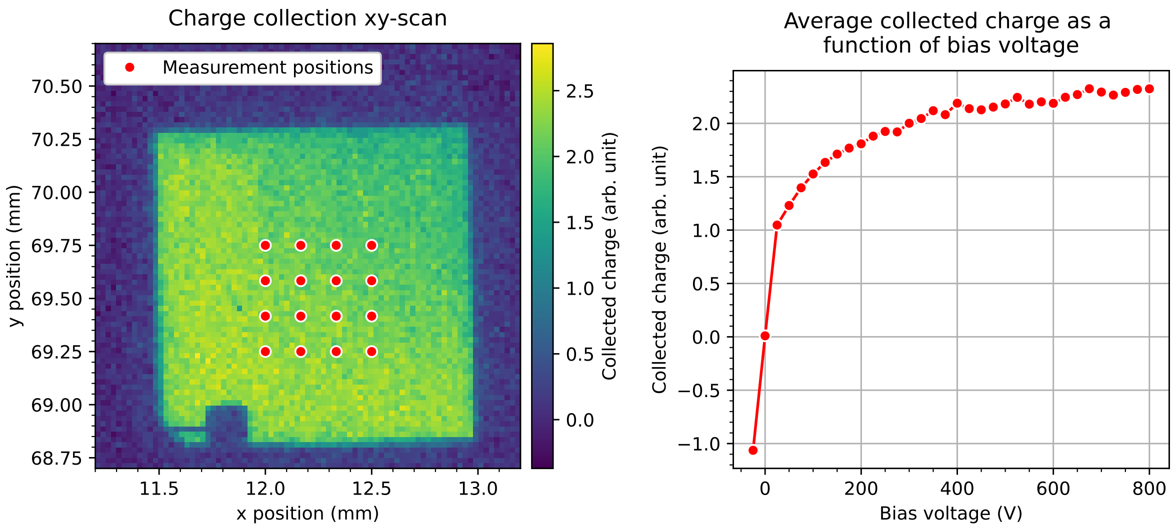

Figure 45: 10^{14} p/cm^2 sensor, with measurement positions and collected charge at different bias voltages.

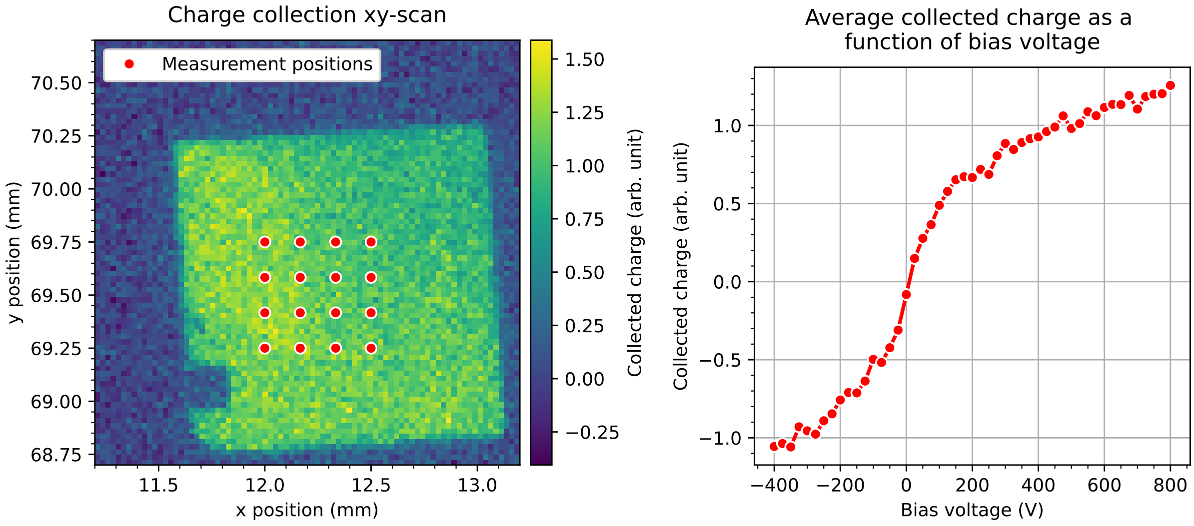

Figure 46: 10^{15} p/cm^2 sensor, with measurement positions and collected charge at different bias voltages.

H Signals for Reverse Biased Sensor

This appendix shows examples of signals from different points on an unirradiated sensor. Figure 47 shows locations of measurement positions and figure 48 shows the corresponding signals. The colors match in both figures.

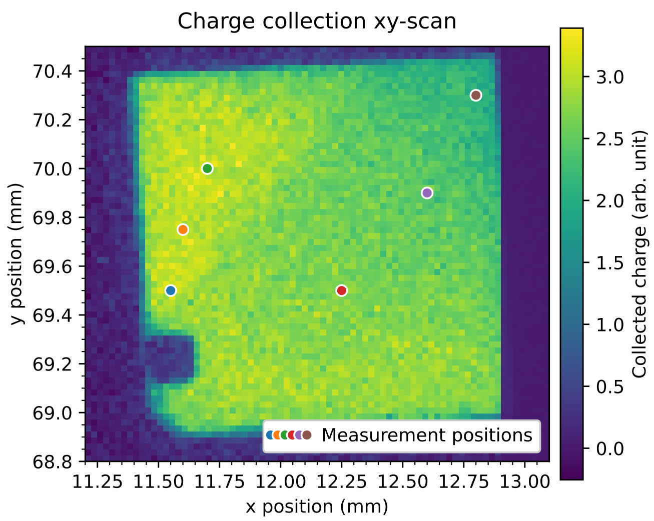

Figure 47: Measurement positions for signals.

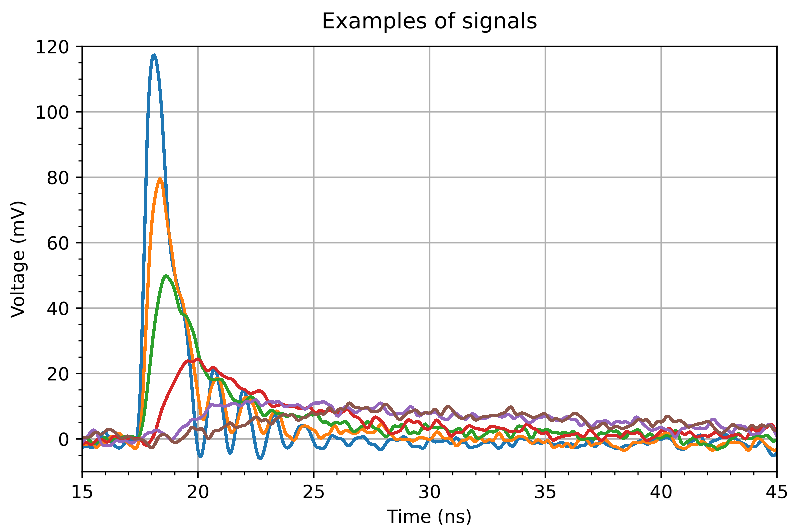

Figure 48: Signals from the measurement positions.

I Charge Collection Temperature Dependence

This appendix shows how charge collection changes with temperature for a 50 µm SiC sensor. Figure 49 shows measurement positions and charge collection curves. Figure 50 shows the average of charge collection between 600-800 V as a function of temperature. A linear fit is also done.

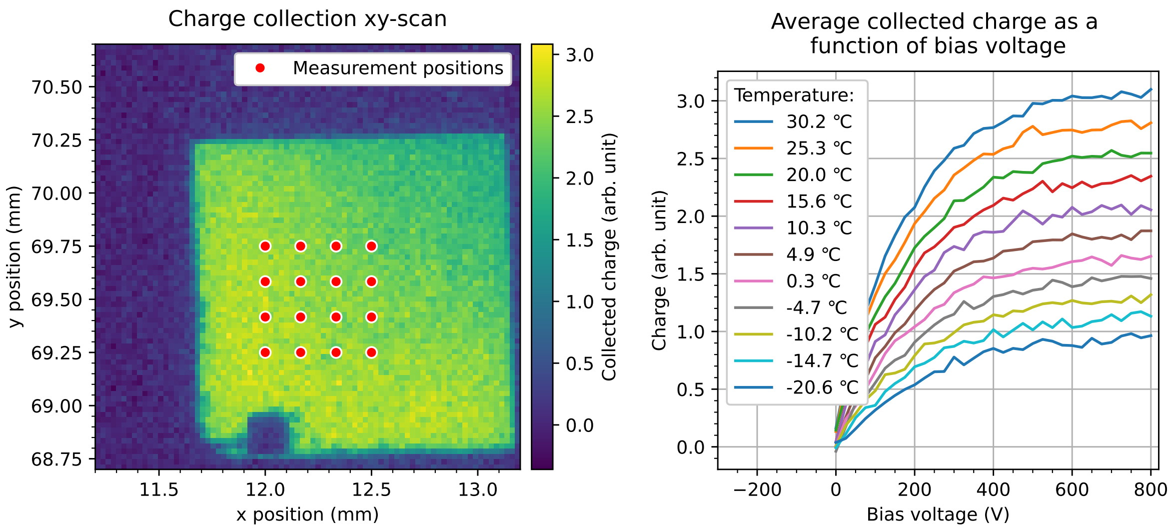

Figure 49: Measurement positions and charge collection for different temperatures.

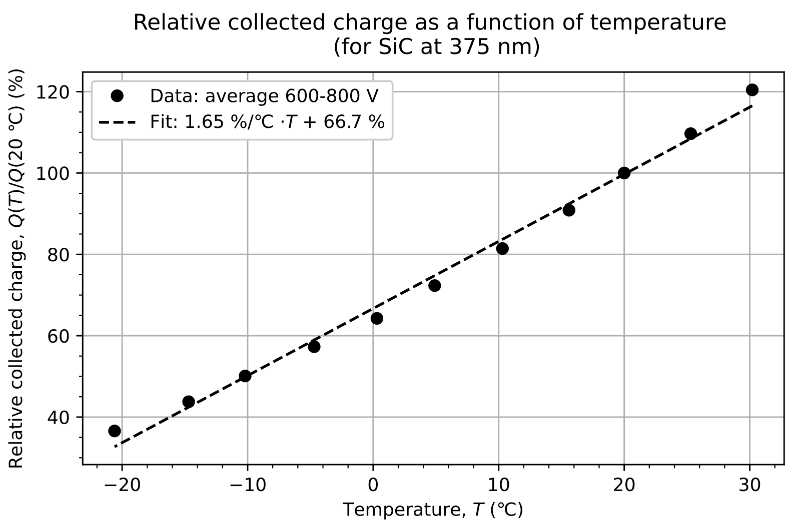

Figure 50: Relative charge collection efficiency as a function of temperature for unirradiated 50 µm SiC sensors.

J Charge Collection Position Dependence

This appendix shows how the measured charge collection depends on the location choice of the 4-by-4 measurement grid on the sensors. Figure 51 is for unirradiated sensor 1 and figure 52 is for unirradiated sensor 2. Note that some measurement positions were almost outside of the sensor in figure 52, which caused the charge collection curves to be lower than expected.

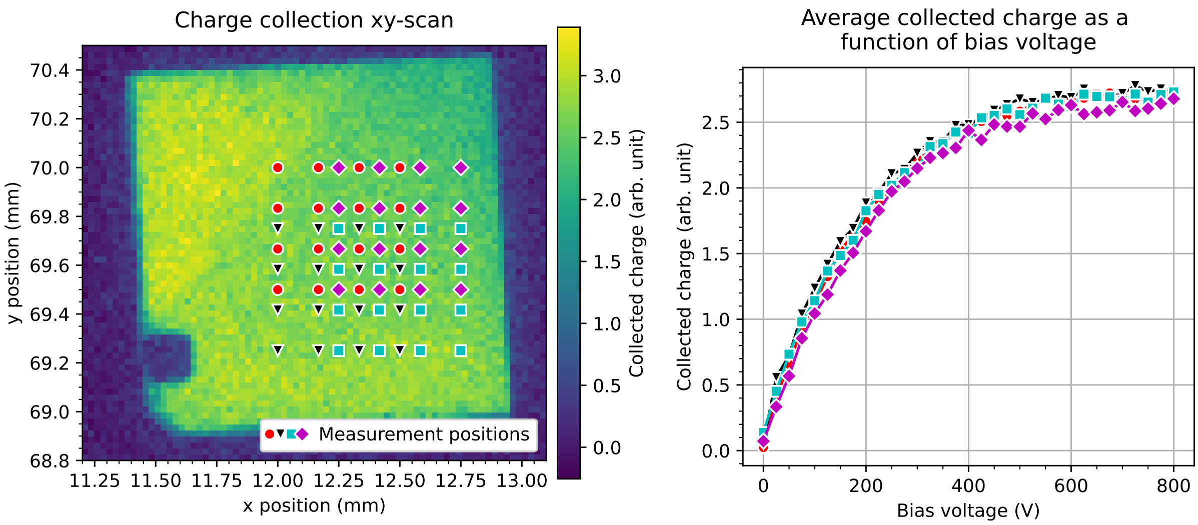

Figure 51: Charge collection for different measurement positions on unirradiated sensor 1.

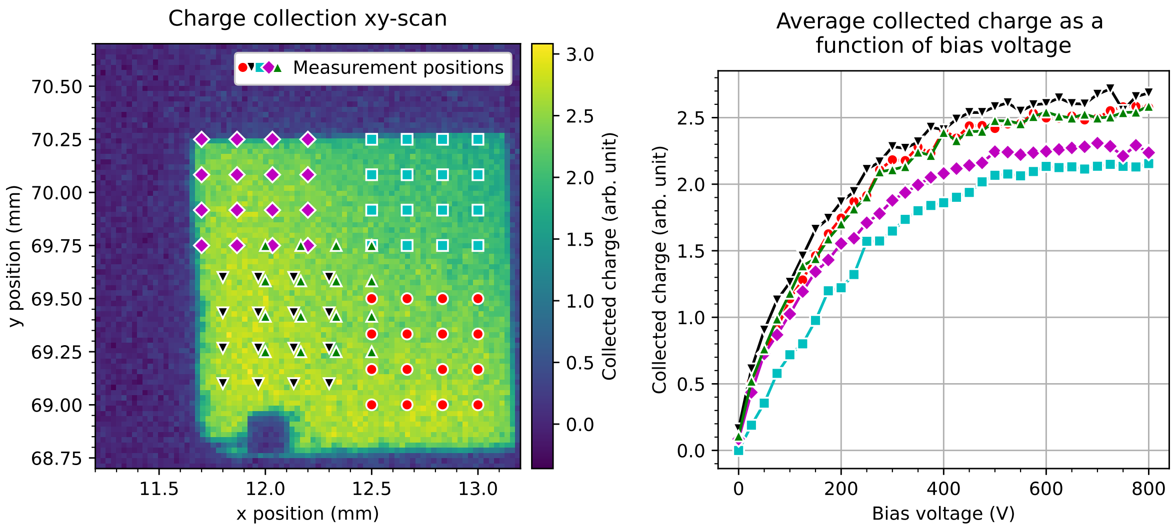

Figure 52: Charge collection for different measurement positions on unirradiated sensor 2.

K Signals for Reverse and Forward Biased Sensor

This appendix shows the signal shape for the forward and reverse biased 10^{15} p/cm^2 sensor. The shapes look the same except for opposite polarity. The signals are averages for the 16 measurement positions on the sensor.

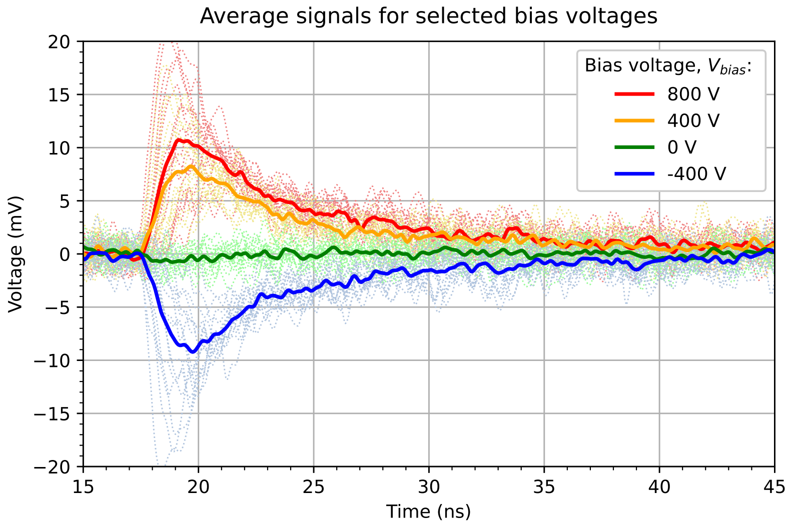

Figure 53: Signals for different bias voltages on the 10^{15} p/cm^2 sensor. The bold lines are averages of the 16 measurement positions, which are the weak lines in the background.